Uppsala University

Independent Project in Engineering Physics

Calibration of Coincidence Gamma Spectrometry Detector GeCo

Authors:
Ellen Ivarsson Biebel & Rasmus Wallentin

Uppsala University, Division for Applied Nuclear Physics
Alva Myrdal Centre for Nuclear Disarmament

Supervisors:
Dr. Peter Andersson & Dr. Erik Andersson Sundén

Abstract

To verify nuclear weapon treaties, such as CTBT the ability to scientifically monitor treaty violations is of importance. One tool for monitoring nuclear weapons testing is the use of gamma ray spectrometry. A calibration on a multi detector element coincidence gamma spectrometer setup was performed from previously gathered experimental data. Data from one calibration sample and a blank sample were analyzed in this project. The first part consisted of energy, full width half maximum (FWHM) and efficiency calibrations, for each of the detectors. Spectra were created, showing the results in the different detectors. From the spectra, several radionuclides were identified, both background nuclides and nuclides from the calibration sample. To each peak, a Gaussian shaped curve was numerically fitted and the parameters were used to perform the calibrations. Efficiencies were calculated for the individual peaks, whereas the energy and FWHM calibrations resulted in linear relationships. During the second part of this project, coincident gamma-rays were investigated. The efficiency for a coincident decay in each detector pair was calculated. This was compared with the product of the singular efficiencies, and a correction term was introduced. Furthermore, the signal to noise ratio was compared for spectra created with different data sorting methods.

Contents

Introduction

Ever since the first nuclear weapon was used in 1945 and the cold war started in 1947, there have been discussions about nuclear safety and nuclear disarmament. The first international political proposal limiting nuclear weapons was proposed and discussed in the United Nations in 1946. USA put forward the Baruch plan which in short proposed scientific transparency from the USA regarding nuclear power, in exchange for letting the United Nations atomic energy commission monitor the usage and for the receiving countries to pledge not to build nuclear weapons. The Soviet Union denied the proposal since they did not like the idea that only the United States would have the ability to build nuclear weapons. Since then, many other treaties have been proposed, one of which is the comprehensive nuclear test ban treaty (CTBT). CTBT bans all nuclear weapons testing. The treaty was adopted by the general assembly in 1996, however, currently 9 countries need to ratify the treaty of which three also need to sign it before it can come in to effect [8] [9] [25].

To verify compliance by the member states with CTBT a verification regime has been setup. The verification system consists of three different parts. Firstly, there are 337 stations creating the international monitoring system (IMS), at which different monitoring techniques are used. Hydroacoustic detectors are used to detect sounds in the ocean, infrasound is used to listen above ground, seismic technologies are used to detect shockwaves spread through the ground and radionuclide monitoring is used to find unusual radioactivity in the air. There is also an international data center (IDC) analyzing data received from IMS and distributing both the analysis and the raw data to every member state. The final component consists of on-site inspections (OSI) that can be carried out to collect evidence if data from IMS indicate a treaty breach once CTBT has taken effect [9].

After detonation of nuclear weapons certain radionuclides are released and spread via air. Detection of higher levels of specific nuclides can thus be used to prove a violation of the CTBT. 72 of the IMS stations are certified nuclear radionuclide stations that rely on noble gas detectors and radioactive particle detectors. The latter work by collecting air samples from filtering aerosols. The samples are then analyzed using gamma-ray spectrometry to determine its contents [3].

Alva Myrdal Centre (AMC) for nuclear disarmament researches the whole nuclear disarmament process from preconditions and hurdles in the field of peace and conflicts to the more technical part of implementation and verification. To spread their knowledge and raise awareness about nuclear disarmament AMC arranges workshops and conferences as well as teaching about the subject. Alva Myrdal Centre was established by Uppsala University in 2021. Project group four of AMC is focused on developing technical tools for nuclear disarmament applications, with competence within applied nuclear physics. Current research revolves around analyzing and modelling sensitive radionuclides and the nuclear fuel cycle. Moreover research regarding techniques for verification of nuclear disarmament treaties like the aforementioned is carried out [7] [21].

A measurement for evaluating the performance of a gamma-ray spectrometer is the minimum detectable activity (MDA). MDA is the smallest activity of a radionuclide in a sample that generates a statistically significant impact in the data for it to be considered detected. MDA is drastically affected by background radiation from the surrounding environment, creating a noise level through which the interesting radiation in the sample must statistically penetrate. To reduce the impact from background radiation, the detection setup can be shielded with dense materials absorbing the background. However the nuclides in the sample also contribute to noise in the data, which may hide other interesting nuclides.

Another technique for reducing the impact from background noise and improving the minimum detectable

activity is studied in project group four at Alva Myrdal Centre, under the name GeCo. Certain radionuclides decay in cascades which produce coincident gamma-rays. A setup with several detector elements is able to detect the coincident gamma-rays in different elements. Since the probability of detecting two coincident gamma-rays from noise is small, the purpose of such a setup is to find only the coincident events and make coincident decays from the sample more apparent compared to background noise [3].

1.1   Problem Description

This project aims to calibrate a multi-detector element setup of 5 different high purity Germanium detector (HPGE) elements. The setup was done under the GeCo project and performed by project group four of Alva Myrdal Centre. Measurements on a few calibration samples were done before the project start. Now data will be analyzed to perform the calibrations necessary to understand the characteristics of the detector. There will be full width at half maximum, energy and efficiency calibrations for all detector elements. Two different approaches for energy calibration and two different approaches for efficiency calibration will be attempted and their results compared. Additionally, this project aims to investigate the peak-peak efficiency for one pair of coincident gamma events. The resulting coincidence efficiency will be compared to the efficiencies of the single detector calibrations to find a possible connection between the two.

Background

Before continuing, there is some background information needed to understand the remainder of the project. It is also a necessary foundation for putting the project in a perspective and understanding its intents.

2.1 Radioactive decay

Before presenting the details of radioactive decay a few definitions are required. Nucleons are the particles that make up a nucleus, namely protons and neutrons. Electrons are not nucleons, since they are not part of the nucleus. Nuclide refers to both the nucleus and the associated electrons. The number of neutrons in a nucleus is denoted by N and the number of protons by Z. The mass number is given by $A = N + Z$. Thus the state of a nuclide can be described in the following manner $^{A}_{Z}\mathrm{Sy}$, or $^{A}\mathrm{Sy}$, since the number of protons is given by the chemical symbol (Sy). A radionuclide is a nuclide with the ability to decay. During radioactive decay the radionuclide splits into products. The sum of the product masses are always smaller than the mass of the original nuclide and the corresponding energy change can be calculated according to $\Delta E = \Delta m \cdot c^2$. Therefore there will always be some extra energy released during decay, which is distributed to the products in a manner proportional to the inverse of their respective masses, such that the lightest products receives the majority of the decay energy. The original nuclide configuration is sometimes refereed to as parent and the new configuration as daughter [11].

2.1.1 Alpha Decay

The alpha (α) particle consists of two protons and two neutrons, equivalent to a Helium-4 nucleus, $^{4}_{2}\mathrm{He}^{+}$. α decay occurs when an alpha particle is emitted from a nucleus and is the preferred type of decay for atoms with high atomic number. α decay leads to a decrease in mass number of four, $A \rightarrow A - 4$, and a decrease of two in atomic number, $Z \rightarrow Z - 2$. The energy released during alpha decay is split between the α particle and the daughter nuclide. Due to the conservation of momentum the difference between the two energies will depend on the difference in mass. There is no neutrino to catch some of the momentum and therefore the α particle will have the same energy each time a certain decay happens. For heavier nuclides, α decay will often lead to daughters in an excited state which results in gamma emission when the daughters return to the ground state as a result [11].

2.1.2 Beta Decay

During beta (β) decay the mass number is always preserved, a so called isobar event. The nuclide along an isobar (constant mass number) with the smallest energy is considered stable, while surrounding nuclides on the isobar β decay until the stable nuclide is achieved. During β^{-} decay a neutron (n) in the nucleus is converted to a proton (p), an electron (β^{-}) and an antineutrino ($\overline{\nu}$), denoted $n \rightarrow p^{+} + \beta^{-} + \overline{\nu}$. An example is Cobalt-60, which decays to Nickel-60 according to $^{60}\mathrm{Co} \rightarrow {}^{60}\mathrm{Ni} + \beta^{-} + \overline{\nu}$. The released energy is mainly occupied by the electron and antineutrino, since they are lightest. β^{-} decay takes place for nuclei with relatively many neutrons compared to the number of protons. There is also β^{+} decay in which a proton is converted to a neutron, a positron and a neutrino, described by $p \rightarrow n + \beta^{+} + \nu$. Positrons are antimatter and

they will be retarded by surrounding matter until they are annihilated by electrons, releasing two photons. β^+ decay is common for nuclides with relatively few neutrons [11].

2.1.3 Gamma Emission

Gamma (γ) emission is a result of transitions between excited states in nuclei. Such an excited state occurs because nucleons can be arranged in different quantized energy levels within the nucleus, much like electrons in their different shells. A nucleus is in an excited state when a nucleon is in a higher level state than the ground state and the de-excitation of this state gives rise to gamma emission. Gamma emission is electromagnetic radiation in the higher energy spectrum with wavelengths smaller than 10^{-10} m, with some overlap with high energy X-ray. X-rays are created from excited electrons, separating them from gamma rays. Gamma emission is not a form of decay like alpha or beta and there are no changes in mass number or atomic number. The only purpose of gamma emission is to rid the surplus energy due to excitation.

Gamma emission is often a bi-product of alpha or beta decay. Both alpha and beta decay can result in a daughter nuclide in its excited state. When that daughter is de-excited, gamma emission occurs. The energy of the gamma particle, the photon, is characteristic for different elements. Often, there are several cascading gamma emissions when an excited nuclide returns to its ground state in several steps. If the middle state has a short half life, there will be no noticeable delay and the two emissions are coincident.

Due to their precisely defined energies, gamma rays are an important tool for identifying nuclides. However, there is some ambiguity in the identification of nuclides. A majority of these are caused by peaks being closer to each other than the resolution of the detector and would disappear if the resolution of the energy measurements were improve. That is however, highly unlikely to be achieved. Situations in which it is entirely impossible to discriminate between nuclides can also appear. This happens when isobaric nuclides decay to the same product. Since the gamma radiation is from the daughter nuclide, it will be the same regardless of which parent was involved in the beta decay. They can only be distinguished by their differences in half life, however this will not be visible for shorter measurements [11].

2.1.4 Gamma Radiation - Interactions

Gamma radiation interacts with matter, which makes it detectable. Note that gamma radiation and X-rays are both electromagnetic radiation with an overlap in energy range, hence they are not distinguishable to a detector. It is possible to detect gamma-rays (and X-rays) because they transfer their energy to electrons within the detector. The electron is then excited, losing its energy by ionization or excitation of the atom which creates an electron-hole pair. These electron-hole pairs can, depending on the detector material, be presented as an electrical signal. The attenuation coefficient reveals how much the gamma radiation is weakened by passing through a material. The coefficient depends on the energy of the gamma-ray and what material it passes through. Some materials are more suitable than others, one of the better is Germanium which will be used in this project. The energy transferred to an electron is the energy absorbed by the detector which is related to what is measured. This energy can be transferred in different ways, three of which are relevant for regular gamma-ray spectroscopy [12].

Photoelectric Absorption

Photoelectric absorption is the dominant energy transfer method at low energies. During photoelectric absorption, the gamma-ray interacts with a bound electron, which is then released. The atom is left in an excited state and can be de-excited in one of two ways. It can distribute the excitation energy among the remaining electrons possibly leading to more ejected electrons and more energy being absorbed by the detector. The de-excitation can also happen when a higher-level electron falls in and takes the ejected electron's place emitting an X-ray in the process. The X-ray, with a little less energy than the gamma-ray, is then absorbed by another atom and the process repeats itself until all the energy is absorbed. During each iteration, part of the energy is retained by the atom due to the conservation of momentum.

During photoelectric absorption, the released electron can come from any of the electron shells, most likely K, depending on the energy of the incident gamma-ray. Because the electron energies are quantized, there will be a discontinuity in the absorption curves with absorption edges at the binding energies for each electron shell.

During the process there is some probability that part of the energy escapes from the detector in the form of fluorescent X-rays, so called X-ray escape. The loss gives rise to an energy peak at lower energy. The peaks are only relevant for small detectors and low photon energies [12].

Compton Scattering

Compton scattering mainly happens for mid-range energies. It occurs when a photon collides with an electron and transfers part of its energy to the electron. The energy transferred to and absorbed by the electron varies with the angle of scattering between the photon and the electron, between zero for the scattering angle $0°$ and a maximum value for the scattering angle $180°$. The maximum absorption is less than the full energy of the incident photon and there will be a continuum of energies between zero and the maximum value with a gap between the maximum value and the incident photon energy. The so called Compton edge at the highest Compton energy will not be straight due to the possibility of the electron having some initial binding energy. The probability for Compton scattering depends mainly on the density of the detector material. Theoretically singular Compton events will create a shape in the spectrum corresponding to figure 2.1b [12].

Pair production

Pair production requires high energy gamma-rays. The gamma-ray interacts with the entire atom and within the coulomb field of the nucleus, the photon converts to an electron-positron pair. Due to this conversion, the incident energy must be at least the mass of an electron-positron pair, namely 1022 keV, however, the process can only be observed if the initial photon energy is even higher. The excess energy that is not converted to mass is equally distributed between the electron and the positron then transferred to the detector medium as they slow down. The positron will, having slowed down enough, annihilate with an electron giving two photons of 511 keV energy, which then interacts with the material in one of the aforementioned ways. Due to the time resolution of the detector, the annihilation will be considered instantaneous [12].
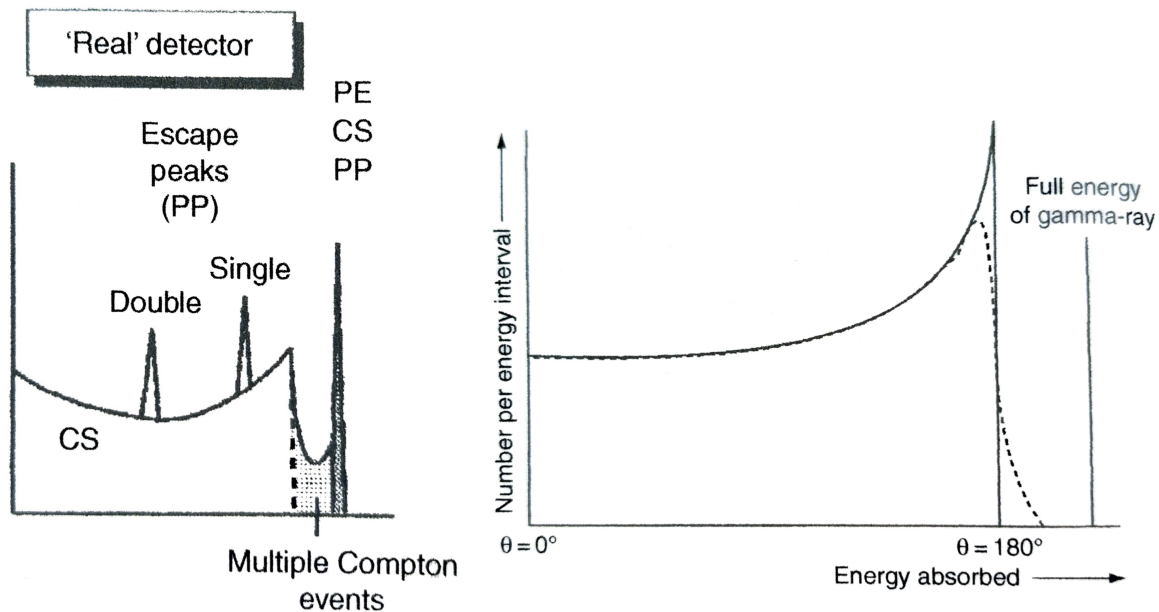
(a) The theoretical spectrogram from decays of equal energy registered by the detector.

(b) The theoretical distribution of Compton scatter events for different singular energies absorbed by the detector.

Figure 2.1: Spectra with the discussed interactions [13].

2.2 The Detector

In order to perceive radioactive decay and gamma radiation, a detector is needed. Here the focus will be on a Germanium detector for gamma-ray spectrometry. In general, the detector material is a semiconductor material.

2.2.1 Interactions Within the Detector

There are two extremes for which there are easily defined interactions, the very large where the boundary is negligible and the very small where only one reaction can happen at a time. A real detector lies somewhere in between and is the only detector relevant for real-world applications and will hence be the only thing discussed here with some characteristics in the detector response and their causes.

A Compton continuum is a continuum of likely energy measurements due to Compton scattering events for different energies between zero and the Compton edge, as illustrated in figure 2.1b. The Compton edge is where the Compton continuum ends, often in a steep manner. The Compton continuum emerges because of the limited size of the detector. After a gamma photon has collided and scattered with an electron, the photon leaves the detector again, leaving only a part of the energy to be absorbed by the electron within the detector. How much energy is measured depends on the scattering angle and there will be a continuum attributed to the many possible angles.

Above the Compton edge, there are some registered emissions due to multiple Compton events, as seen in figure 2.1a. This happens when the Compton scattered photon has continued Compton interactions with other electrons before it leaves the detector, resulting in a higher energy measurement than a single Compton scattering event thus allowing energies between the Compton edge and the full energy top.

After pair production, the positron annihilates with an electron and two photons are created. These photons have specific energies of 511 keV, one of these can be completely absorbed while the other leaves the detector, resulting in a peak in the spectrum at 511 keV below the full energy peak, called the single escape peak. Naturally there is a corresponding double peak at 1022 keV below the full energy peak for the case where both photons immediately leave the detector. The single and double escape peaks will create their own peaks in the spectrum, as seen in figure 2.1a.

The full energy top is the top that can be seen when the entire gamma-ray energy is absorbed by the detector. This mostly happens when the photon is photoelectrically absorbed, either directly or after Compton scattering or pair production. It can also happen if there is multiple Compton scattering until all energy is absorbed or if both photons stay within the detector and transfer all their energy after pair production. Larger detectors allow the gamma-ray to transfer more of its energy and give larger full energy peaks. This gives rise to the shaded peak in figure 2.1a [12].

2.2.2 Detection and Semiconductors

When gamma rays interact with matter, energetic electrons are created. To measure the energy of a gamma ray, the energy of the electrons must be measured. Semiconductors are the only reasonable material for such a task. Free atoms have electrons in orbitals associated with certain energy levels. Combining several atoms into a structure, the discrete energy levels turn into continuous energy intervals, called energy bands. The highest energy interval a non excited electron can occupy is called the valence band and the next higher energy interval is called the conduction band. For semiconductors the valence band is normally filled and electrons can only enter the conduction band if they are excited, leaving behind a hole in the valence band. Other valence electrons can move into the hole, making the hole seemingly move. Electrons in the conduction band can move around in the structure and thus if an electric field is applied they will move towards the positive end. Holes will appear to move to the negative cathode in an electric field. The movement of the holes and conduction electrons can be registered as a current. Energy bands are a property of all materials, however only semiconductors have an energy gap of suitable size between valence and conduction band.

The highly energetic electrons created by the gamma rays, scatter and excite the other electrons in the semiconductor, creating electron-hole pairs. The primary excited electron from the gamma ray can and will excite electrons lying in energy bands below the valence band to energy states above the conduction band. This is not problematic since deep holes move up to the valance band and more energetic electrons scatter

again until all holes and excited electrons lie in the valence and conduction band respectively, without loss of energy. If the energy absorbed by the material is E_{abs} and the energy needed to create one electron-hole pair is ε the total number of electron-hole pairs is E_{abs}/ε. An electric field is applied over the semiconductor in intervals, sweeping away the electron-hole pairs. This can be detected as a current proportional to the number of electron-hole pairs, which in turn is proportional to the absorbed energy. Hence, the registered current is a measurement of the absorbed energy [14].

Detectors are manufactured with a protective cap around the Germanium crystal, commonly made from Aluminium. During manufacture of Germanium crystals, a dead layer of impure Germanium is also created. Both the detector cap and the dead layer will shield the Germanium crystal from gamma rays and only some photons transmit through both layers. The transmission fraction is decided by the thickness, material and energy of the photon. For Germanium detectors shielded by Aluminium caps gamma transmission fractions vary widely for energies between 30 and 110 keV [14].

Theory

The purpose of gamma-ray spectrometry is to determine which radionuclides exist in a studied sample and their activity. Measurements are performed by placing the sample in the detector and detecting the emitted gamma rays. The energy of the gamma ray is detected in the form of an electrical signal, the strength of which is proportional to the energy of the gamma ray. As described in section 2.2 the set of signals is discrete (a specific current strength is called channel) and the number of times they are registered during the measurement is counted (called number of counts or just counts). A spectrum can be plotted with the channel on the x axis and the number of counts on the y axis. Radionuclides emit gamma rays with characteristic energies, giving rise to peaks in the spectrum. From the peaks, the qualitative content of the sample can be decided. To determine the activity the following equation is needed.

$$C = \varepsilon I_\gamma A T \tag{3.1}$$

Multiplying activity (A) with the duration of measurement (T) gives the total number of decays. The intensity (I_γ) is the probability that the specific energy gamma ray is emitted during a decay. The number of counts in the net peak is denoted C and corresponds to the number of times an event with a specific energy has been registered in the detector. Thus the efficiency (ε) is the probability that the gamma ray deposits all of its energy in the detector. [15]

To be able to determine the content of an unknown sample, the characteristics of the detector must be known. The channels need to be related to the gamma energy in an energy calibration. The efficiency is characteristic for every detector and the geometrical setup, moreover it varies with the energy of the gamma ray. Finding the relation between efficiency and energy is called efficiency calibration.

3.1 Calibrations

Calibration is the process of characterizing a detector and its traits. The characterization is necessary for using the detector in applications. Descriptions of the performed calibrations are given below.

3.1.1 Energy Calibration

In an energy calibration the conversion between channel and energy is found. Measurements are performed on a sample with known content properties and the known decay energies are paired with the peaks seen in the uncalibrated spectrum. The mean channel of the peak is extracted and an energy vs channel plot is generated. To finish the calibration a curve is fitted through the points. Usually a line is enough to describe the relationship, but sometimes a quadratic term is necessary. [15]

3.1.2 Efficiency Calibration

An efficiency calibration aims to find the relationship between efficiency and energy. Rewriting equation (3.1) and defining $c = \frac{C}{T}$ as the number of counts per second the following equation is obtained.

$$\varepsilon = \frac{c}{A I_\gamma} \tag{3.2}$$

The efficiency can thus be calculated, if the number of counts per second (c) is known. Using error propagation the standard deviation in efficiency is given by equation (3.3), since none of the variables are correlated.

$$\sigma_\varepsilon = \sqrt{\left(\frac{1}{AI_\gamma} \cdot \sigma_c\right)^2 + \left(\frac{c}{I_\gamma A^2} \cdot \sigma_A\right)^2 + \left(\frac{c}{AI_\gamma^2} \cdot \sigma_{I_\gamma}\right)^2} \tag{3.3}$$

An example of a completed efficiency calibration showing the typical behaviour is presented in figure 3.1. Low energy gamma rays get absorbed by the protective layer surrounding the germanium crystal and by the dead layer that forms on the crystal when it is produced. This generates an approximately linear relationship in the low energy region. Gamma rays with higher energies are not effected by these two layers and instead the behaviour is determined by the rate of compton scattering events. Gamma rays with high energies are more likely to compton scatter and leave the detector and thus the photo peak efficiency decreases for higher energies. In the intersection, called a knee, the two behaviours superpose and generate a curve [15].
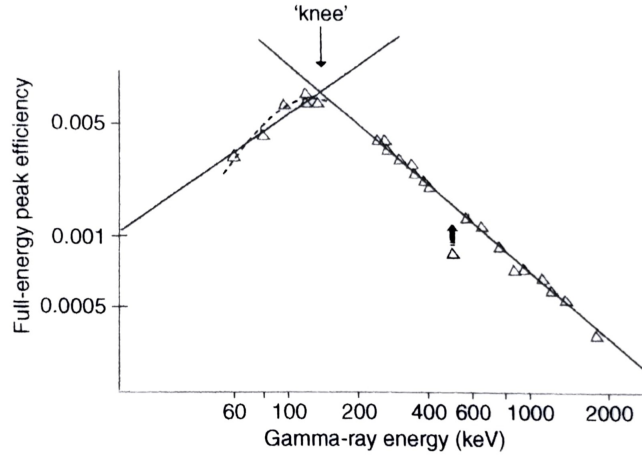

Figure 3.1: Example of an efficiency calibration. The point lying beneath the curve is from the 511 keV annihilation peak [16].

3.1.3 FWHM Calibration

The full width at half maximum (FWHM) measurement determines the resolution of the detector. The full width at half maximum is the width of the peak at half of the peaks maximum value. The quantity is depicted for a Gaussian curve in figure 3.2, and in this case FWHM is $x_2 - x_1$. For a Gaussian curve it is also possible to calculate FWHM analytically with (3.4) [20].

$$\text{FWHM} = 2\sqrt{2\ln 2} \cdot \sigma \approx 2,355\sigma \tag{3.4}$$

Similar to the other previously mentioned calibrations, FWHM is calculated for each peak and the data points are visualised in a FWHM vs energy plot and regression is used to find the relationship.
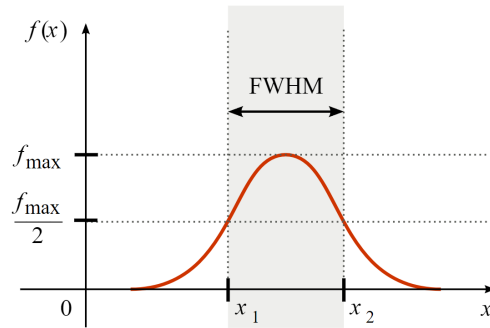

Figure 3.2: Illustration of full width at half maximum measurement [22].

3.2 Poisson Statistics and Error Propagation

To practically extract information from a spectrum, the net peak and background must be modeled. Net peak here refers to the counts belonging to a specific gamma decay energy. The measured number of counts in a single channel mathematically follows a Poisson distribution for both the peak and the background. Thus the number of counts registered in one channel during measurement is a number drawn from two superposed Poisson distributions. The standard deviation of a Poisson distribution is the square root of its mean value and for two superposed Poisson distributions it is the square root of the sum of their mean values. The counts in one channel in a region of interest (a region in which a peak exists) is $C = C_b + C_p$, where C_b is the counts from the background and C_p is the counts from the peak. Thus the standard deviation in the counts belonging to a channel is $\sigma_C = \sqrt{C_b + C_p} = \sqrt{C}$. For large means Poisson distributions can be approximated as Gaussian distributions and the background in a region of interest is approximately linear [18]. The data in a region of interest can thus be modeled as a line with a superposed Gaussian,

$$f(x) = ae^{-\frac{1}{2}\left(\frac{x-\mu}{\sigma}\right)^2} + kx + m \tag{3.5}$$

where each data point has a standard deviation equal to its square root.

The uncertainty of a quantity A calculated from $A = f(x, y, z...)$ is in a first order approximation given by the following expression.

$$\sigma_A = \sqrt{\left(\frac{\partial f}{\partial x}\right)^2 \sigma_x^2 + \left(\frac{\partial f}{\partial y}\right)^2 \sigma_y^2 + \left(\frac{\partial f}{\partial z}\right)^2 \sigma_z^2 + 2\frac{\partial f}{\partial x}\frac{\partial f}{\partial y}\sigma_{x,y} + 2\frac{\partial f}{\partial x}\frac{\partial f}{\partial z}\sigma_{x,z} + 2\frac{\partial f}{\partial z}\frac{\partial f}{\partial y}\sigma_{z,y} + ...} \tag{3.6}$$

Where the derivatives are evaluated at the mean and σ_x is the standard deviation in x and $\sigma_{x,y}$ is the covariance of x and y [4].

3.3 Half Life and Decline in Activity

Decay and radioactivity can be described mathematically. The rate of disintegration, called activity, is the rate of which a parent radionuclide decays into its daughter nuclide, measured in number of disintegrations per second, called Becquerels. The activity changes with time.

The decay rate (A), the rate of change in the number of atoms of a nuclide, is proportional to the number of atoms of a nuclide present in the sample (N). The relationship is described as

$$A = -\frac{dN}{dt} = -\lambda N \tag{3.7}$$

where λ is the decay constant. Useful relationships are $1/\lambda = \tau$ and $\lambda = \ln(2)/T_{1/2}$, where τ is the average lifetime of the nuclide and $T_{1/2}$ its half life. This results in the following expressions for the number of atoms, N_t, and the activity, A_t at time t.

$$N_t = N_0 e^{-\lambda T} \tag{3.8}$$

$$A_t = A_0 e^{-\lambda T} = A_0 e^{-\frac{\ln(2)}{T_{1/2}}T} \tag{3.9}$$

The subscript 0 corresponds to time $t = 0$. Performing error propagation for the parameters relevant for the experiment on relation (3.9) yields:

$$\sigma_A = \sqrt{\left(\frac{\partial A}{\partial A_0}\right)^2 \sigma_{A_0}^2 + \left(\frac{\partial A}{\partial T}\right)^2 \sigma_T^2} =$$

$$= \sqrt{\left(e^{-\frac{\ln(2)}{T_{1/2}}T}\right)^2 \sigma_{A_0}^2 + \left(A_0 e^{-\frac{\ln(2)}{T_{1/2}}T} \cdot \frac{\ln(2)}{T_{1/2}}\right)^2 \sigma_T^2} \tag{3.10}$$

3.4 Coincidence Spectrometry

To increase sensitivity in the measurements of radioactive nuclides, a technique called coincidence spectrometry is used. Some radioactive decay processes generate several gamma ray emissions in a small time interval, these are called coincident gamma rays. An example of such a nuclide is ^{60}Co which decays through β^- into ^{60}Ni. When the excited ^{60}Ni nuclide falls to its ground state it commonly passes through an intermediate energy level, as seen in the decay scheme in figure 3.3a, releasing two gamma rays of different energies in a small time interval. In the conducted study a sample containing the coincidence gamma ray emitter ^{134}Cs is analyzed, whose decay scheme is presented in figure 3.3b. In the following section, the theory of coincident gamma rays and how such detection data behaves are discussed. A coincident event is henceforth defined as an event where two different detector elements both detect an energy deposit within a time interval of 400 nanoseconds.
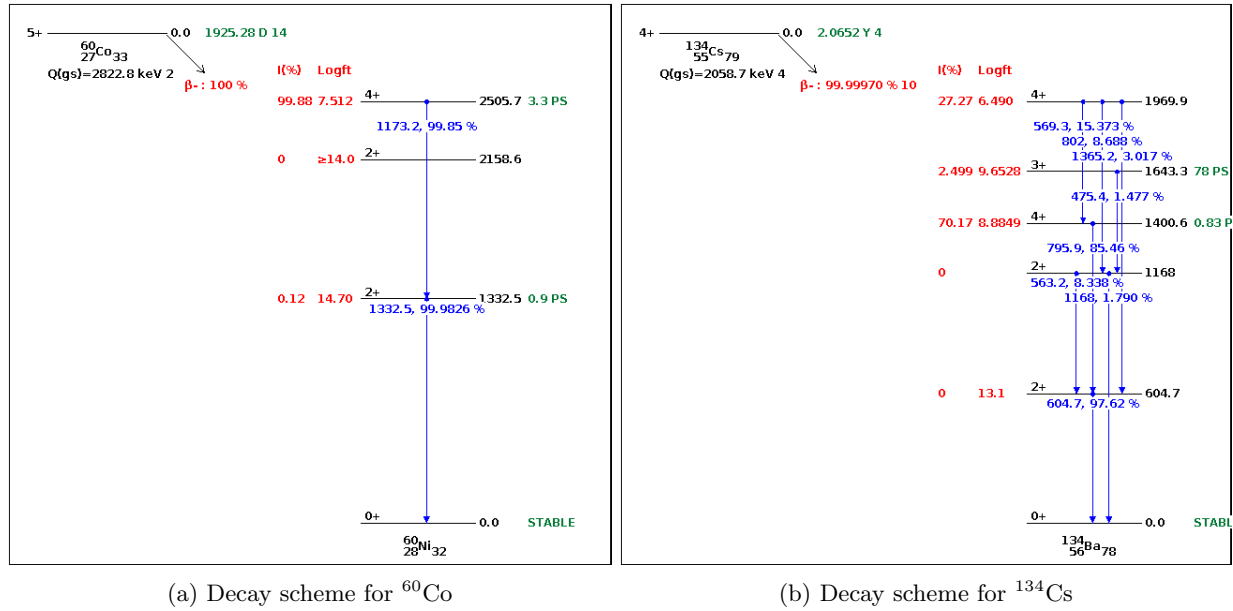

(a) Decay scheme for ^{60}Co   (b) Decay scheme for ^{134}Cs

Figure 3.3: Decay scheme for ^{60}Co (left) and ^{134}Cs (right). Only gammas with intensities larger than 1% are shown. Observe that both of these have coincident gammas [5]

.

In single spectrometry histograms, the channel data for singular detectors is studied. For coincidence spectrometry, a pair of detectors must be considered simultaneously, then a 2D histogram can be generated. The 2D histogram has the channels from one detector along one axis and the channels of the other detector along the other axis. An example of such a plot is found in figure 3.4. The data is from a measurement of a sample with a radionuclide with coincident gamma ray decay. Especially coincident gamma rays of energies 605 and 796 keV around channels 3500 and 4500 are common. The first observation of interest is the two lines creating a box around channels 3500 in the two detectors. Both of these lines appear because one detector has registered a full energy deposit at channel 3500 and the other a Compton scattering event from the coincident gamma ray. Compton scattering is common for this type of detector. The same phenomena explains the lines at channel 4500. In this case, one of the detectors have registered a decay at channel 4500 and the other registers a Compton event from the less energetic coincident gamma ray. The second thing to note is the tilted purple line crossing both axes at around channel 3500. The detectors are placed close to each other and the photon leaving one detector after undergoing Compton scattering can enter the other detector. When the gamma ray deposits some of its energy in one detector and completely deposits the remaining energy in the other detector, the event must take place along this line. Mathematically the line is described by $E = x + y$, where E is the energy of the original gamma ray, x the energy deposited in the first detector and y the energy deposited in the second detector. Such events are common and therefore present
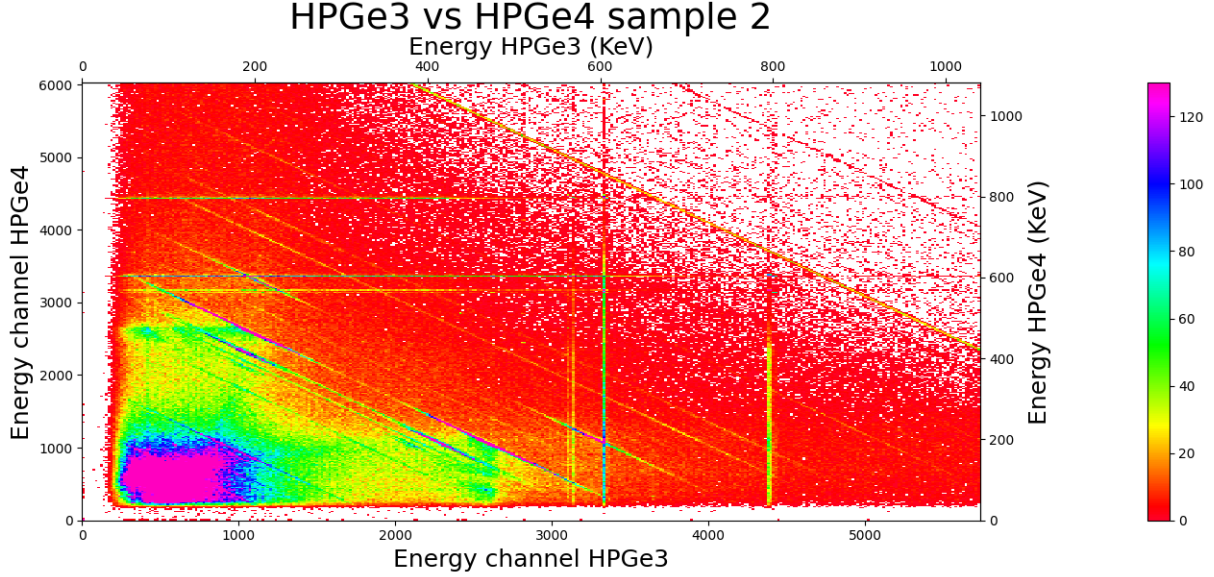
in the histogram.

Figure 3.4: A 2D histogram created from experimental coincidence data from the experiment described later. Specifically this is data from detectors HPGe3 and HPGe4 from the calibration sample. Observe that the histogram is zoomed to an area where coincident decays take place. For visualization purposes each histogram bin (point) covers an interval of channels.

Focusing attention again to the diagonal line in the histogram, it is observed that the line is more present towards the edges and fades in the middle. The reason for this is the geometry of the setup. During a Compton scattering event the energy deposited is decided by the scattering angle, where an angle of 180° (the photon travels in opposite direction after scattering) deposits the highest amount of energy and a small scattering angle (photon path is close to unchanged) deposits the least amount of energy. For a photon to scatter from one detector to another the interval of angles is, for geometry reasons, limited. Thus only certain angles and energy deposits can give rise to a point along this line. The next thing to observe are the green areas located a little closer to the origin than the previously discussed line. These are created from photons Compton scattering in one detector that then scatter once more in the other detector and then leave the system. Such a photon deposits some of its energy in the detectors and then leaves with a bit of energy left. Mathematically this can be described by $E - E' = x + y$, where E' is the energy of the photon after scattering in both detectors. The final observation is the large pink area close to the origin. This is background noise in combination with low energy Compton scattering events.

In this study the peak-peak coincidence efficiency was of interest. The peak-peak efficiency refers to the event where both gamma rays fully deposit their energies in different detectors. For example ^{134}Cs can undergo a decay process where two gamma rays are released at energies 605 and 796 keV. A peak-peak event for this pair of gamma rays is when one detector registers 605 keV and another detector registers 796 keV. The efficiency of such an event is calculated with an expression resembling that of the single efficiency. The number of times two coincident gamma rays are released by the nuclide is the product $A \cdot I_{\gamma_1,\gamma_2} \cdot T$. Where A is the activity, I (intensity) the probability that both energies are coincidentally released given that the nuclide decays, and T the time duration of measurement. The specific efficiency is the probability that detector x detects gamma energy a and detector y detects gamma energy b given that coincident gamma rays are released. This efficiency is denoted $\varepsilon_{a,b}^{(x,y)}$. The number of detected coincident events of this sort is denoted $C_{a,b}^{(x,y)}$ and is also referred to as the number of counts. Thus the coincidence efficiency is calculated with equation (3.11) [1].

$$\varepsilon_{a,b}^{(x,y)} = \frac{C_{a,b}^{(x,y)}}{A \cdot I_{\gamma_1,\gamma_2} \cdot T} \tag{3.11}$$

For example the efficiency of the data shown in figure 3.4, with decay energy 796 keV (channel 4500) detected in detector 3 and decay energy 605 keV (channel 3500) detected in detector 4 is denoted $\varepsilon_{796,605}^{(3,4)}$. The counts associated to this efficiency ($C_{795,605}^{(3,4)}$) lie in the peak located at the intersection of channels 4500 and 3500.

It is possible to express coincidence efficiency in terms of single efficiencies through probability theory. Coincidence efficiency is the probability of detecting gamma ray a in detector x and detecting gamma ray b in detector y, Which can be calculated using [1]

$$\varepsilon_{a,b}^{(x,y)} = \varepsilon_a^x \cdot \varepsilon_b^y \tag{3.12}$$

Equation (3.12) assumes that detecting gamma ray a in detector x and detecting gamma ray b in detector y are independent events. This is not the case since there might be a correlation in direction and instead a correction term is introduced in the equation below.

$$\varepsilon_{a,b}^{(x,y)} = \varepsilon_a^x \varepsilon_b^y \cdot \rho_{a,b}^{(x,y)} \tag{3.13}$$

$\rho_{a,b}^{(x,y)}$ can be found with equation (3.14) and its standard deviation is given by equation (3.15).

$$\rho_{a,b}^{(x,y)} = \frac{\varepsilon_{a,b}^{(x,y)}}{\varepsilon_a^x \varepsilon_b^y} \tag{3.14}$$

$$\sigma_{\rho_{a,b}^{(x,y)}} = \sqrt{\left(\frac{1}{\varepsilon_a^x \varepsilon_b^y} \cdot \sigma_{\varepsilon_{a,b}^{(x,y)}}\right)^2 + \left(\frac{\varepsilon_{a,b}^{(x,y)}}{\varepsilon_a^x (\varepsilon_b^y)^2} \cdot \sigma_{\varepsilon_b^y}\right)^2 + \left(\frac{\varepsilon_{a,b}^{(x,y)}}{(\varepsilon_a^x)^2 \varepsilon_b^y} \cdot \sigma_{\varepsilon_a^x}\right)^2} \tag{3.15}$$

Method

The aim of this project was to find the energy scale for each detector, the single detector efficiencies, and coincidence efficiencies. The experiment was performed before the start of this project and hence data was available. The experimental setup is described in section 4.1. Before any data analysis took place, all relevant radionuclide data (such as half life , decay energies, coincidence decay energies etc.) from the nuclides in the calibration samples was gathered and compiled in a spreadsheet. This spreadsheet and corresponding calculations are available in appendix A.1. In this project, two different approaches of modelling the net peak in the spectra were examined. The first uses a curve fitting algorithm to find the Gaussian shape, described in section 4.3. The other is a more arithmetic approach described by D. A. Gedcke and presented in section 4.4. A comparison between the different methods of extracting the net peak counts was performed and the results are available in section 5.2.1 and 5.2.2. The curve fit approach in ROOT was deemed the most reliable, thus the final single calibrations were completed with ROOT. For the coincidence efficiencies only one pair of coincident gamma ray energies were studied. The methodology for extracting the net peak counts from the coincidence data set is similar to the methodology described by D. A. Gedcke, however some data manipulation was necessary, as described in section 4.6.

4.1 The Experiment

A detector arrangement was set up at Ångström laboratory and measurements were performed by the supervisors before the start of the project. The arrangement is depicted in figure 4.1 and consists of five germanium detectors. Four detectors were placed as close as possible to the sample and another detector was placed on top of the sample. A few Bismuth Germanate (BGO) detectors were placed between the sample and the top detector. These are not relevant for this project and will not be considered further. Note in figure 4.1b that detector 3 and 4 are located opposite each other and closer to the sample than detector 1 and 2. Detector 5 is located the furthest away and is also shielded by the BGO detectors. The detectors require cooling and were each connected to an insulated container filled with liquid nitrogen (the large cylinders with caps). A sample consists of a filter that has been folded and compressed, in order to minimize its size, the filter is then placed in a small cylindrical plastic can. The plastic can was placed in the middle of the setup seen in figure 4.1b during measurements.

As previously mentioned, each detector records the amplitude of an electrical signal corresponding to a certain energy. This information was transferred to a data collection device, which also had an internal clock and gave each data point an individual timestamp determining the time in picoseconds since the beginning of the measurement. The final data thus consisted of three components; the time stamp, the channel corresponding to the measured energy and the number of the detector recording the energy. The data was stored in .root format, which is a format used at CERN. The data format has been developed by CERN and is especially made for analysing large amounts of data from particle detectors. To read .root files, the ROOT data analysis framework must be used. Measurements were performed on four different samples, two calibration samples, one empty sample and sample only containing ^{60}Co. The contents and relevant properties of the nuclides in the calibration samples are presented in appendix A.1. For reasons related to the execution of the measurement on calibration sample 1 it will not be analyzed further in this report. The sample containing ^{60}Co was only used for the qualitative analysis described in the following section.
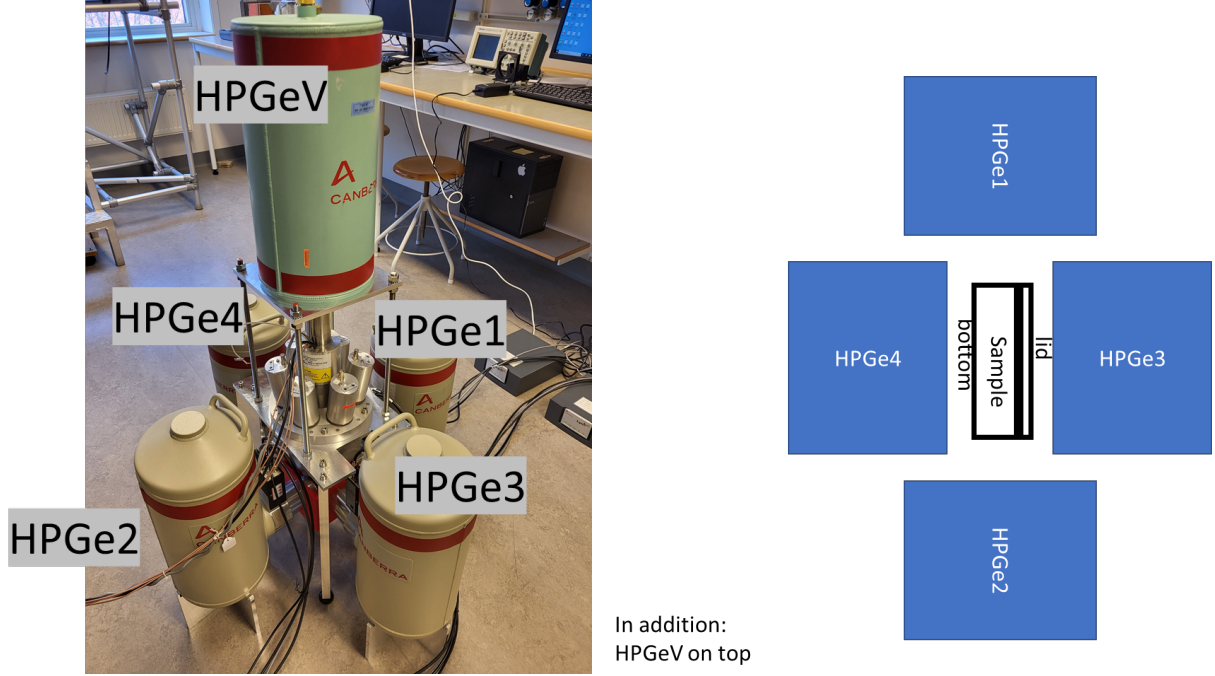
(a) Overview of the setup. The large cylindrical containers are filled with liquid nitrogen, each cooling one detector. The detector elements can be seen as metallic cylinders entering the red box in the middle.

(b) The sample placement under the top detector.

Figure 4.1: Placement of detectors and sample in the GeCo setup [2]
.

4.2 Data Observations

To formulate the following methods for data analysis, a few observations of the data must be considered. Firstly, the peaks in the spectra were identified. To achieve this the sample with ^{60}Co was observed next to the empty sample where the two decays energies from ^{60}Co were clearly visible. A first linear approximation of the energy vs channel relationship was made from the ^{60}Co peaks and used to identify the other peaks in the spectrum. Both peaks from nuclides in the sample and peaks from commonly measured background radiation were found. It must be noted that the number of peaks observed from the sample was sparse. On the other hand there was a lot of identified surrounding background radiation. The identified background radiation can be used in addition to the radiation from the sample to perform the energy calibration. However, background radiation can not be used for the efficiency calibration since the activity of the sources were unknown. This leaves only a few peaks for the efficiency calibration, not enough to represent the efficiency relationship across the entire energy spectrum of the detector. However, the individual efficiencies are still known and can be used when studying the coincidence behaviour.

The second notable observation of the data is the appearance of surrounding background peaks. In figure 4.2 the intervals containing the energy corresponding to ^{241}Am 59,4 keV and ^{134}Cs 563,3 and 569,3 keV energies are visualised from detector 1 for both calibration sample 2 and the empty sample. Comparing figures 4.2c and 4.2b it is clear that there exists surrounding background radiation that will boost the ^{134}Cs 563,3 and 569,3 keV peaks. However comparing figures 4.2a and 4.2b no such background is observed. Surrounding background radiation could in this case be radiation from materials in the laboratory or radiation existing in the sample holder or filter. Subtraction of this background radiation must be performed when evaluating the number of counts in a peak for the efficiency calibration in the peaks were such interference is present.
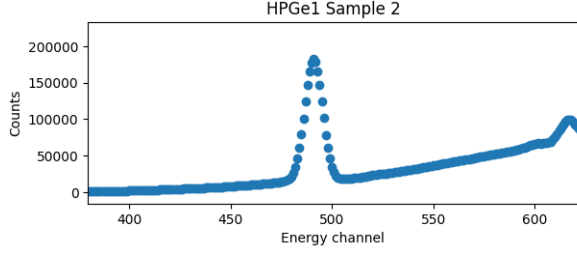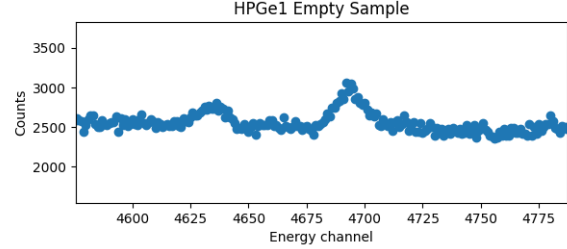
(a) The spectrum at the location of the ^{241}Am 59,4 keV peak in calibration sample 2.
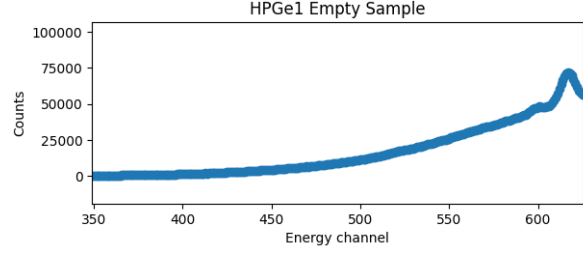
(b) The spectrum at the location of the ^{241}Am 59,4 keV peak in the empty sample.
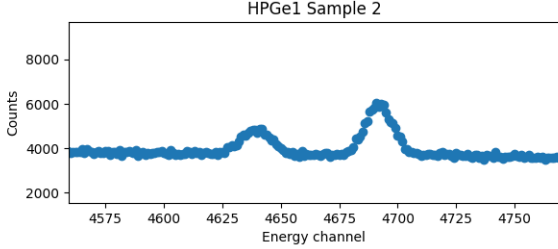
(c) The spectrum at the location of the ^{134}Cs 563,3 and 569,3 keV peaks in calibration sample 2.

(d) The spectrum at the location of the ^{134}Cs 563,3 and 569,3 keV peaks in the empty sample.

Figure 4.2: Parts of the spectra recorded in detector 1 from calibration sample 2 (left) and from the empty sample (right). Note that the duration of measurement for sample 2 and the empty sample is different and that the figures are quantitatively different.

4.3   Curve Fit Approach

This method aims to model the Gaussian peak in the spectrum through numerical curve fitting algorithms and then analytically find the necessary quantities for the calibrations. To find the Gaussian curve, two different methods were tested, one using the ROOT data analysis framework and one converting data from ROOT format and using SciPy. For both methods, spectra were created and for each peak of interest, a channel interval containing the peak was defined. Using the intervals, a curve fitting algorithm was used to find the Gaussian shape of the peak and the linear background. An initial guess of the parameters for the function was passed to the curve fitting algorithms. The curve fitting algorithms returned the optimal parameters and the covariance matrix for the parameters, also containing the variance of the parameters themselves. With the correct arguments, the statistical error in the number of counts described in section 3.2 could be passed to the algorithms and was reflected in the covariance matrix.

ROOT

The data originally came in .root format suitable for ROOT, thus histogram plots of the spectrum were made directly from the data files. A function of the form (3.5) was created and passed to the curve fitting algorithm. An Initial guess for two parameters were made. The mean (μ) of the peak was the bin with the maximum number of counts in the interval and the standard deviation was set to ten, $\sigma = 10$. By passing the correct argument the curve fit algorithm calculations were made with the statistical uncertainties in the data points. In ROOT the `Fit` function of the histogram class was used.

SciPy

As aforementioned, the data was originally in .root format and to be able to use a SciPy function it must be retrieved in a SciPy friendly format. To achieve this, histograms were created with ROOT and the counts in each bin (channel) were retrieved and stored in a SciPy readable format. The initial guess was made such that μ was the channel with the largest number of counts in the interval, amplitude $a = 200$ and

standard deviation $\sigma = 5$. For the other parameters the initial guess was 1. The SciPy function used was `scipy.optimize.curve_fit`.

Analysis

When the parameters of the function (3.5) and corresponding covariance matrix were known all necessary information for completion of the calibrations was known. The number of counts per second (c) in a peak from a nuclide of interest was calculated by integration, equation (4.1), and the error approximated by equation (4.2)

$$c = \frac{1}{T} \int_{-\infty}^{\infty} ae^{-\frac{1}{2}\left(\frac{x-\mu}{\sigma}\right)^2} dx = \frac{\sqrt{2\pi}}{T} a\sigma \tag{4.1}$$

$$\sigma_c = \frac{\sqrt{2\pi}}{T} \sqrt{(a \cdot \sigma_\sigma)^2 + (\sigma \cdot \sigma_a)^2 + 2cov[\sigma, a] \cdot a\sigma} \tag{4.2}$$

For the case where background subtraction was necessary, the registered number of counts per second (cps) was calculated by subtracting the cps from the sample measurement with the cps from the empty sample. Thus the cps from the sample nuclide was given by equation (4.3), where index s indicates values from the sample measurement and index e values from the empty sample. Error propagation of (4.3) gives (4.4).

$$c_c = c_s - c_e = \sqrt{2\pi} \left(\frac{a_s \sigma_s}{T_s} - \frac{a_e \sigma_e}{T_e} \right) \tag{4.3}$$

$$\sigma_{c_c} = \sqrt{2\pi} \sqrt{\left(\frac{\sigma_s}{T_s}\sigma_{a_s}\right)^2 + \left(\frac{a_s}{T_s}\sigma_{\sigma_s}\right)^2 + 2cov[a_s, \sigma_s]\frac{a_e\sigma_s}{T_e^2} + \left(\frac{\sigma_e}{T_e}\sigma_{a_e}\right)^2 + \left(\frac{a_e}{T_e}\sigma_{\sigma_e}\right)^2 + 2cov[a_e, \sigma_e]\frac{a_e\sigma_e}{T_e^2}}$$
$$\tag{4.4}$$

When the cps from the nuclide in the sample was known, the efficiency and its corresponding deviation could be calculated with equations (3.2) and (3.3). For the energy calibration, the mean of the Gaussian (μ) was taken as the channel number corresponding to the energy of the peak. For the FWHM calibration, values were calculated using equation (3.4), since the standard deviation, σ, of the Gaussian was known.

4.4 Gedcke Approach

D.A. Gedcke describes an alternative method for finding the net peak counts in a spectrum, using a simple arithmetic approach. In figure 4.3 intervals are marked to help the reader understand the calculations. A region of interest (ROI) is chosen, containing the entire peak to the extent that any missed counts in the edges of the net peak are negligible,n. The ROI has width η_p. To estimate the background counts two new regions (N_{B1} and N_{B2}) are defined. These are both of equal size and half as wide as the ROI ($\eta_p/2$). Both N_{B1} and N_{B2} are located at equidistant distances (d) from the ROI. The background counts in the ROI (B) is then estimated by summing all counts in N_{B1} and N_{B2} (all green points in figure 4.3), which together create an interval of the same width as the ROI. Assuming that the background is linear, the mean of the background regions is the same as the mean background in the ROI. The net peak counts (C) is calculated by summing all counts in the ROI (the blue and purple points in figure 4.3) and subtracting the estimation
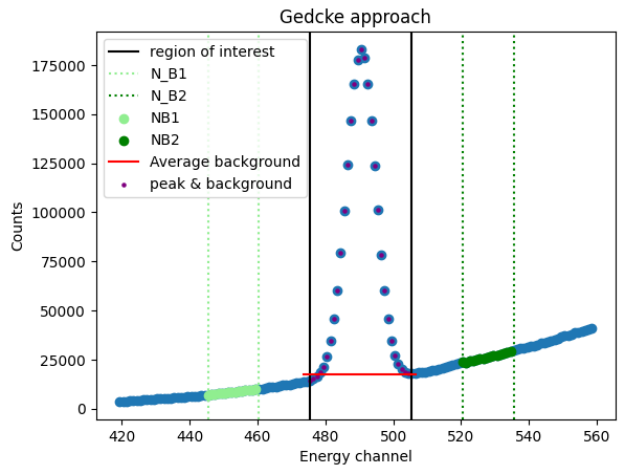

Figure 4.3: Visualisation of Gedckes method.

of the background. If the total number of counts in the ROI is defined as N_T, the calculation is mathematically described $C = N_T - B$. Both N_t and B have uncertainties $\sigma_{N_T} = \sqrt{N_T}$ and $\sigma_B = \sqrt{B}$ since both measurements are drawn from Poisson distributions, as described in section 3.2. The error in net peak counts is therefore given by $\sigma_C = \sqrt{N_T + B}$ [18].

4.5   Completion of Single Calibrations

Energy, efficiency, and FWHM calibrations are completed once the relationship between the desired quantity and energy (eg. channel for energy calibration) are known. The presented values in the results for the finalized calibrations of the individual detectors were extracted using the curve fit approach in ROOT.

Energy Calibration

With the extracted channel-energy pairs from each detector the energy calibration was completed using the SciPy function `scipy.optimize.curve_fit` fitting a line to the data. The following expression need to be found with error estimations for the parameters.

$$E = k \cdot ch + m \tag{4.5}$$

However, the SciPy function only takes errors in the dependent values (y values) and thus a fit to the following expression was performed.

$$ch = k' \cdot E + m' \tag{4.6}$$

Equation (4.6) can be converted to the wanted expression (4.5) through the following relations.

$$k = \frac{1}{k'} \quad m = -\frac{m'}{k'} \tag{4.7}$$

Performing error propagation on the new parameters yields:

$$\sigma_k = \sqrt{\left(\frac{1}{k'^2} \cdot \sigma_{k'}\right)^2} \quad \sigma_m = \sqrt{\left(\frac{1}{k} \cdot \sigma_{m'}\right)^2 + \left(\frac{m'}{k'^2} \cdot \sigma_{k'}\right)^2} \tag{4.8}$$

Energy calibrations were performed individually for each of the five detector elements. Both peaks from the calibration sample and background radiation was used to give a accurate result over a large interval.

Full Width at Half Maximum

FWHM was calculated for peaks originating from nuclides in the calibration sample and background radiation using the relationship between σ and FWHM described in section 3.1.3. FWHM was then plotted on the y-axis with energy on the x-axis to visualize the relationship. A linear function of the following form was fitted to the data.

$$FWHM = k \cdot E + m \tag{4.9}$$

The k and m values achieved for each individual detector are presented in the results.

Efficiency Calibration

Because the activity of the nuclide must be known, only peaks originating from nuclides in the sample were used. Due to the lack of active nuclides in the sample, the efficiency-energy relation could not be found. Instead the point efficiencies were calculated and used in the analysis of coincidence data.

4.6   Coincidence Efficiency

All sets of coincident events for all detector pairs were extracted from the dataset. If two energies were registered within a time interval smaller than 400 ns, the two events were considered to be coincident. Due to the time limited nature of the project, only one pair of coincident decay energies were studied. The two coincident decay energies with the highest intensity in calibration sample 2 were ^{134}Cs energies 604,721 and 795,864 keV with an intensity of 85,3% [3]. Therefore this pair was studied

Coincidence data can be visualized like previously described in section 3.4 and figure 3.4. Another tool to visualise the data is to project the 2D histogram onto one of its axes, creating a one dimensional histogram. In the new 1D histogram, the counts in channel z are all counts registered at channel z in detector x given that any energy is coincidentally registered in the other detector (y). In figure 3.4 if a projection is made onto detector 3 (located on the x-axis) this corresponds to summing the 2D histogram vertically. The result of such an operation can be seen in figure 5.10.

To find the peak-peak counts, a different method must be used. Instead of summing over all channels in detector y, the sum is taken over an interval. This technique is visualized in figure 4.4 and called gating. When extracting gated data like the one in figure 4.4b, the channel interval in the detector which the data is not projected on must be defined. The interval was chosen based on the Gaussian from the single calibrations such that it included all points within a range of 4 standard deviations. The interval can be expressed $[\mu-4\sigma, \mu+4\sigma]$, where μ and σ are the mean channel and the width of the Gaussian peak defined in equation (3.5).
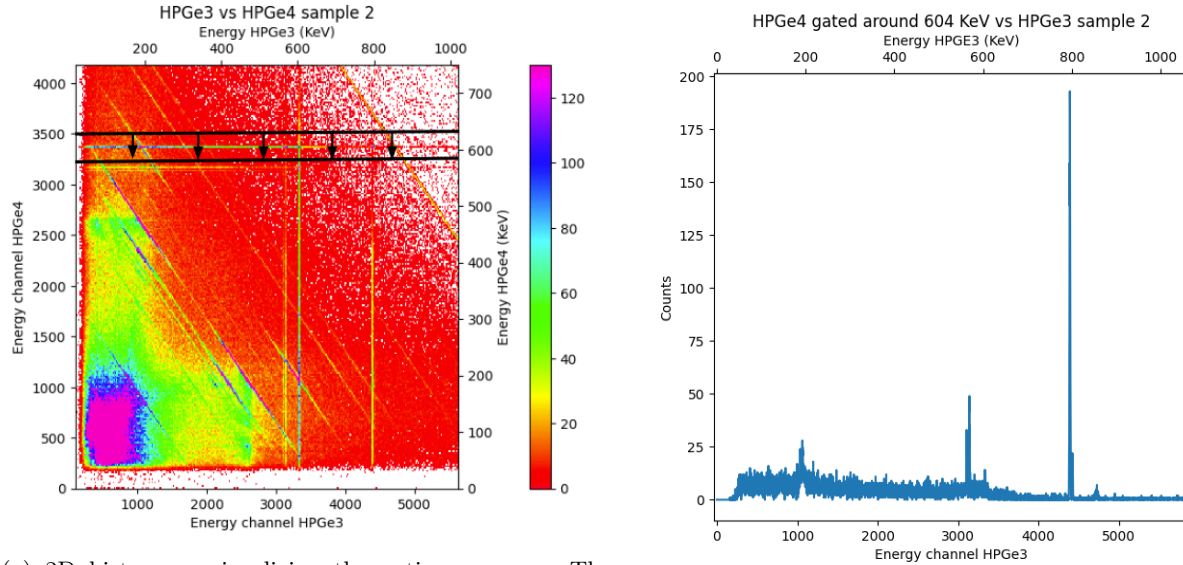
(a) 2D histogram visualizing the gating process. The black lines visualize an exaggerated gating area and the arrows the direction of summing for the projection.

(b) Spectra generated after gating.

Figure 4.4: Both subfigures are made from coincidence data of calibration sample 2 registered in detector HPGe3 and HPGe4. The gating interval visualized in figure 4.4a was made to create figure 4.4b.

Studying the gated spectrum in figure 4.5 the peak does not have the clear Gaussian shape seen in the single detector histograms. Instead Gedckes method was used to find the number of counts and the corresponding uncertainty. Note that ^{134}Cs also has coincident decays of 605 keV and 802 keV, creating the small bump around 802 keV in figure 4.5. Therefore the background intervals were always chosen by hand in order to not include the 802 keV peak in the background regions. Every detector pair has two combinations of detecting coincident decay energies 605 keV and 796 keV. For example 605 keV detected in detector 1 and 796 keV detected in detector 2 or 796 keV detected in detector 2 and 605 keV detected in detector 1. The peak-peak counts were always extracted by gating in the detector with the higher index (HPGe2 is higher than HPGe1) and projecting this onto the detector with the lower index. The efficiencies were

then calculated with (3.11). Since no coincident decays were expected to be detected from surrounding background radionuclides nor found in the empty sample, no background peak subtraction from analyzing the empty sample was performed.
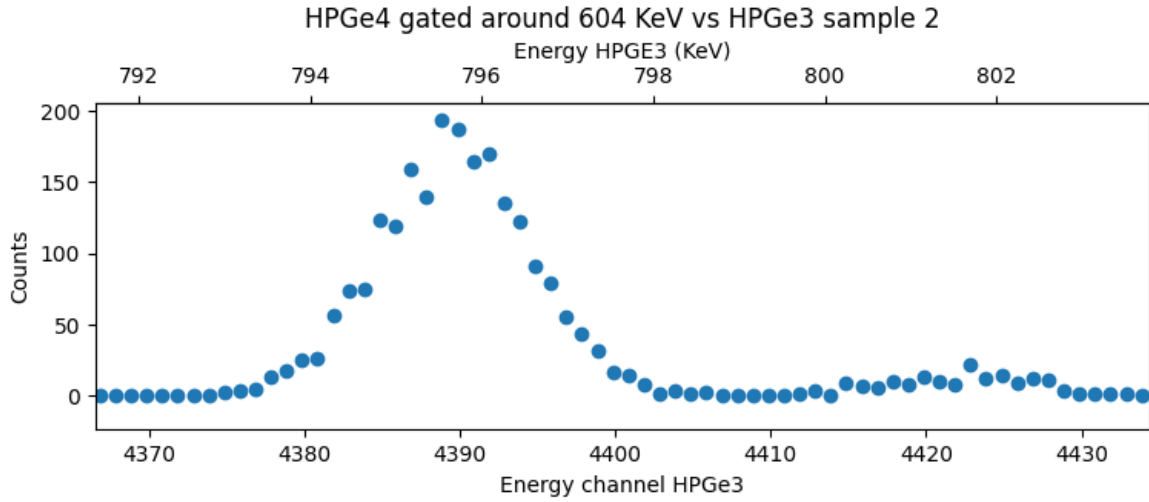

Figure 4.5: Coincidence data between HPGe3 and HPGe4 from calibration sample 2. Gating around 605 keV has been made in the manner described in the text and projected onto HPGe3. The figure is zoomed into an area around 796 keV.

The coincidence efficiencies presented in the results were calculated by extracting the net peak counts using Gedckes method on the gated spectra. This was performed for all detector pairs excluding detector five for ^{134}Cs coincident gamma energies 604,721 keV and 795,864 keV.

Results

In this section, the results from the data analysis described in section 4 will be presented. To begin, there is a description of background nuclides which had significant impact on the measurements. This is followed by the results from the single detector calibration, first a comparison between the different methods of extracting information and subsequently the results of the energy, efficiency and full width half maximum calibrations. Lastly, the results from the coincidence measurements are presented and the results from single and coincidence calibrations are juxtaposed.

5.1 Activity in Background

During the search for and identification of peaks, background activities from the surrounding environment of several energies were found. These background emission events included the common Th-232 decay series and possibly the U-238 decay series, though this was not investigated properly. All background gamma emitting nuclides, that had significant peaks in the spectrum, and their energies are displayed in table 5.1. There were other nuclides with visible peaks but only those significant enough to use for calibration are listed in the table.

Table 5.1: Significant background gamma emitters and their energy

Nuclide	Gamma energy (keV)
K-40	1460,82
Tl-208	583,19
	2614,15
Pb-214	295,22
	351,93
Ac-228	338,32
	911,20
	968,97
Pb-212	238,63

A spectrum with all identified nuclides can be seen in figure 5.1. It can be noted that the number of peaks observed from the sample is sparse, but correspond to the activity calculated from the nuclear data in appendix A.1.

From the spectrum of the blank sample, it was determined that some background radiation interfered with the energies of interest. There was interference with Cs-134 of energies 563,246, 569,331 and 795,864, but not with energy 604,721 keV of Cs-134. Additionally, there was some background interfering with the Cs-137 peak of energy 661,657 keV. It was deduced that the background interfering with the Cs-134 peak of energy 795,864 was from Ac-228 with energy 794,794, several other decay energies belonging to this nuclide were also found. Regarding Cs-137, it is a very common background nuclide and thus likely giving rise also to this background peak. Identification of nuclides creating background peaks at Cs-134 energies were not investigated further.

The background emissions not interfering with interesting energies, were used during the energy calibration. First however, useful data was extracted from all peaks, the result of which is described in the following sections.

5.2 Single Detector Calibration

The single detector calibration was performed for each detector, independently of measurements in any of the other detectors. The first step, plotting a histogram over the measured counts, resulted in the spectrum
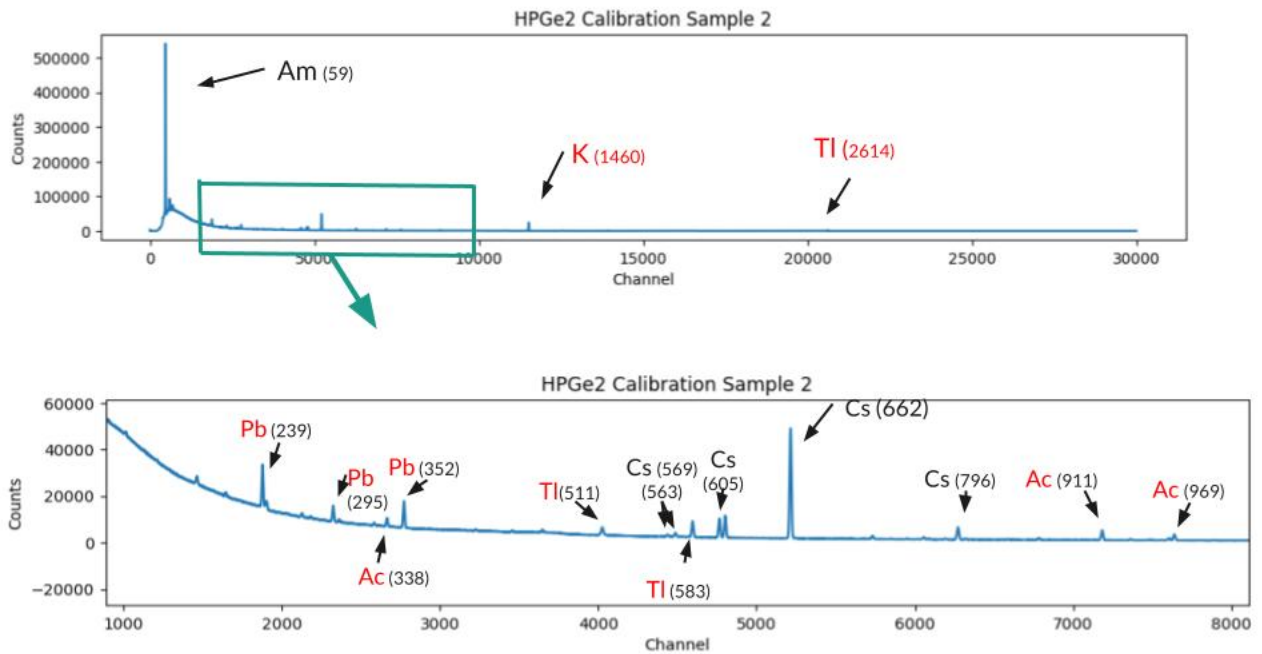
Figure 5.1: Spectra from detector 2 of calibration sample 2, with labels stating which radionuclide the peak belongs to. Black labels state nuclides existing in the sample and red labels are radionuclides in the surrounding background. The decay energy is given in parenthesis in keV. Only the symbol and not the mass number is specified, and thus nothing separates ^{134}Cs from ^{137}Cs except for the energy of their decay.

shown in figure 5.2 This figure portrays the spectrum for detector 1. Several peaks could easily be detected and more were found upon closer inspection.
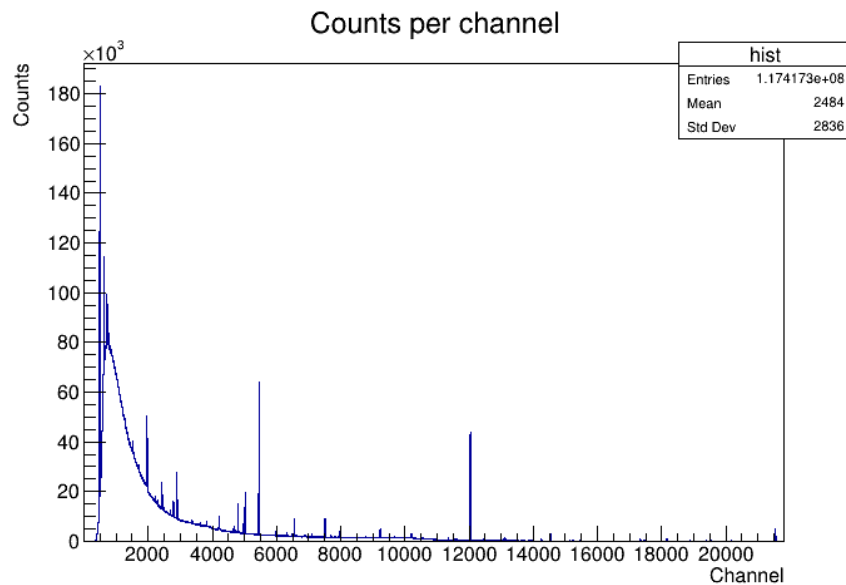

Figure 5.2: A spectrum over the measurements in detector 1

5.2.1 ROOT and SciPy Comparison

Using the curve fit approach described in section 4.3, within suitable intervals for all peaks, it was possibe to fit a well suited Gaussian to all significant peaks. One of those peaks is a result of the 59 keV energy release from Am-241. Two modified Gaussian fits to this peak in detector 1, can be seen in figures 5.3a and 5.3b. The first being a result of the fit using ROOT and the second a result of the fit using SciPy. The fitting of the modified Gaussian function was of the same nature for all significant peaks in all detectors.

The parameters from the fits in the mentioned figures are juxtaposed in table 5.2 which can also be used to compare the two methods. It shoulds be noted that all parameters from the Gaussian part of the fitted function were similar between the two method, they were all within the estimated error of the corresponding parameter from the other fit. The parameters from the linear part of the fitted

Table 5.2: Comparison of a Gaussian fit using ROOT and SciPy.

	ROOT	SciPy
k	180.35919 ± 0.93812	177.40440 ± 0.96215
m	-72490.250 ± 453.726	-71100.336 ± 464.723
a	166663.51 ± 169.82	166675.68 ± 169.33
μ	490.41244 ± 0.00393	490.41394 ± 0.00393
σ	4.3014040 ± 0.003537	4.3046243 ± 0.003504

function were close but not within the estimated errors. Notable is also that the estimated errors for the ROOT fit are smaller for the first two parameters and only slightly larger for the last three. Based on this, it was decided to use ROOT for fitting Gaussian curves to all peaks.
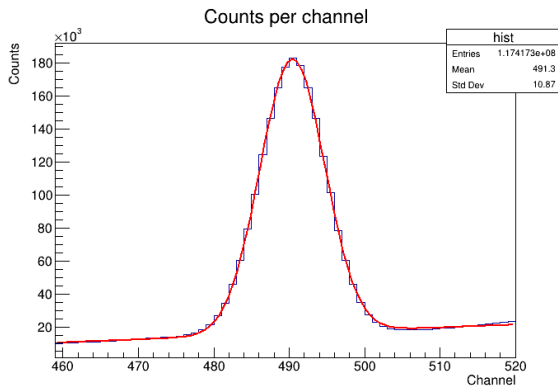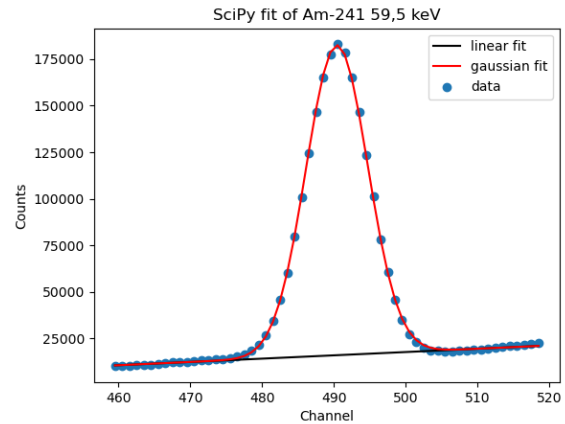

(a) Numerically fitted with ROOT. (b) Numerically fitted with SciPy.

Figure 5.3: Gaussian fits performed with ROOT and SciPy to the 59,5 keV peak of ^{241}Am.

Using the aforementioned fits to do an energy calibration, described in section 4.5, one energy calibration was performed for each of the methods, ROOT and SciPy. They can be seen in figure 5.4a and it can be noted that the values, seen as orange and blue dots in the figure, are almost identical for both methods. A linear function was fitted to both sets of data, the two fits can also be seen in the same figure, a close up can be seen in figure 5.4b where the difference between the two fits is visible. The figures shown correspond to the results of the energy calibrations for detector 1. It must be noted however, that the results were similar for all detectors with almost identical results for ROOT and SciPy. Upon closer inspection, like figure 5.4b, it was noticed that the linear fit using ROOT data points and SciPy data points always differed slightly. Figures for the comparison between the two energy calibrations of the remaining detectors can be found in appendix A.2.

The modified Gaussian fits could also be used when finding the number of counts for the efficiency calibration. The result of which will be described in section 5.2.3.
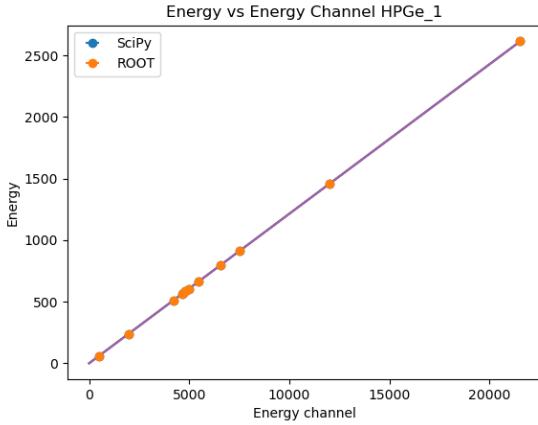
(a) Energy calibration for both ROOT and SciPy.
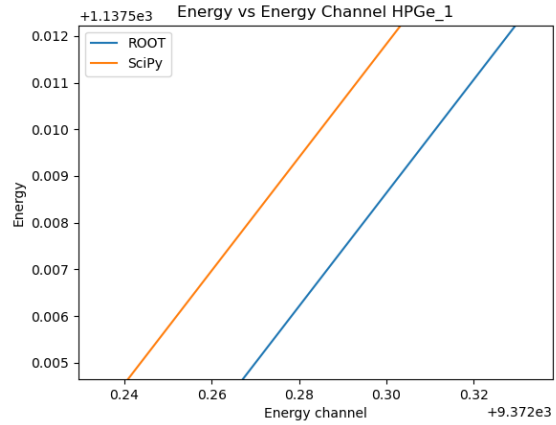
(b) Close-up comparison of ROOT and SciPy.

Figure 5.4: A comparison between a linear regression fit to the ROOT data points and SciPy data points.

5.2.2 Curve Fit and Gedcke Comparison

The curve fit approach with ROOT and SciPy was followed by a comparison to the Gedcke approach described in section 4.4. Analogously, the Gedcke approach for finding the number of counts for an efficiency calibration, was tested and evaluated on the 59 keV Am-241 peak in detector 1. A visual representation of the chosen regions can be seen in figure 4.3 where the method is also illustrated. The region of interest (ROI) was chosen to be between the channels 476 and 506, an interval of $\eta_p = 30$ channels. The regions for determining background counts (N_{B1}

Table 5.3: The estimated number of counts using each method.

Method	Counts in net peak
ROOT	1796969 ± 2929
SciPy	1798446 ± 2909
Gedcke	1754066 ± 1670

and N_{B2}) were consequently chosen to be 15 channels wide and the distance d between the ROI and the background regions was chosen to be 15 channels. The number of counts in the background regions being
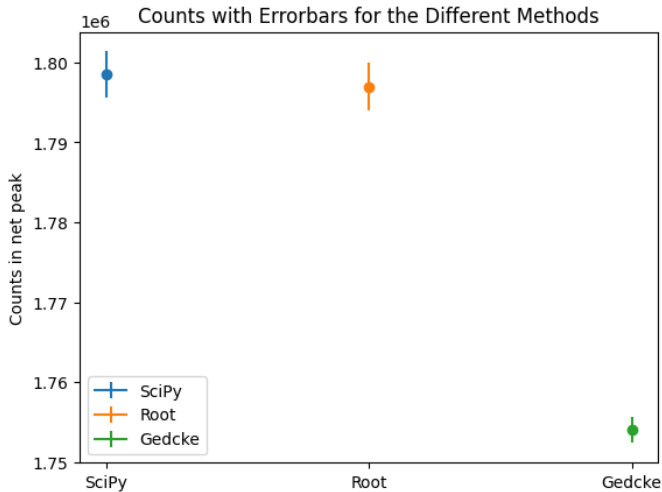
Figure 5.5: A comparison between the number of counts calculated using three different methods.

$N_{B1} = (446, 461)$ and $N_{B2} = (521, 536)$. The number of counts estimated to be in the net peak for the three different methods can be seen in table 5.3 and are visually represented in figure 5.5.

Gedckes method resulted in a lower count rate than ROOT and SciPy that were very close to each other. The curve-fitting methods include a larger part of the net peak, integrating the Gaussian curve from negative infinity to positive infinity whereas Gedckes method limits the area over which the counts are summed. Moving forward, it was decided that curve-fitting using ROOT was the preferred method for both energy calibration and efficiency calculations. This was decided since it takes a larger area of background into account and also because the needed curve fits were readily available from the energy calibrations.

5.2.3 Calibrations

The energy calibration for all detectors are illustrated in figure 5.7. In the figure, the energy corresponding to each channel is plotted for all observed points. The linear regression based on those observations can also be seen. The linear model for the correlation between energy and channel for each detector are compiled in table 5.4.

Table 5.4: The parameters of the linear models achieved by energy calibration.

Detector	k (keV/channel)	m (keV)
1	$0.1213665870890 \pm 7.25 \cdot 10^{-10}$	$-0.024576563 \pm 1.99 \cdot 10^{-6}$
2	$0.126853367189 \pm 1.13 \cdot 10^{-9}$	$-0.0576287016 \pm 8.94 \cdot 10^{-7}$
3	$0.1812708799478 \pm 7.61 \cdot 10^{-10}$	$-0.0372334354 \pm 3.34 \cdot 10^{-7}$
4	$0.1794048521041 \pm 5.91 \cdot 10^{-10}$	$-0.0563389270 \pm 2.43 \cdot 10^{-7}$
5	$0.104918242085 \pm 2.81 \cdot 10^{-9}$	$-0.07707413 \pm 3.35 \cdot 10^{-5}$

To the eye, the plots in figure 5.7 show a linear relationship. Upon investigating this further by plotting the error between the fit and each of the points, it is clear that there is a correlation between error and channel or energy. As an example, the mentioned plot for detector 2 is added in figure 5.6. The remaining detectors had similar plots which can be seen in appendix A.2. It was decided however, that the errors in the fit were small enough to keep the linear fit.

When plotting the full width half maximum (FWHM) together with the energy for each peak, it was observed that the relationship between energy and FWHM could be approximated as linear. Consequently, a linear function was fitted to the points and for each detector, a linear model to predict the FWHM for a specific energy was created. The mea-surements and linear regression for detector 1 can be seen in figure 5.8. The remaining plots can be found in appendix A.2. They have the same general behaviour though individual values vary. The result from the linear fits can be found in table 5.5.
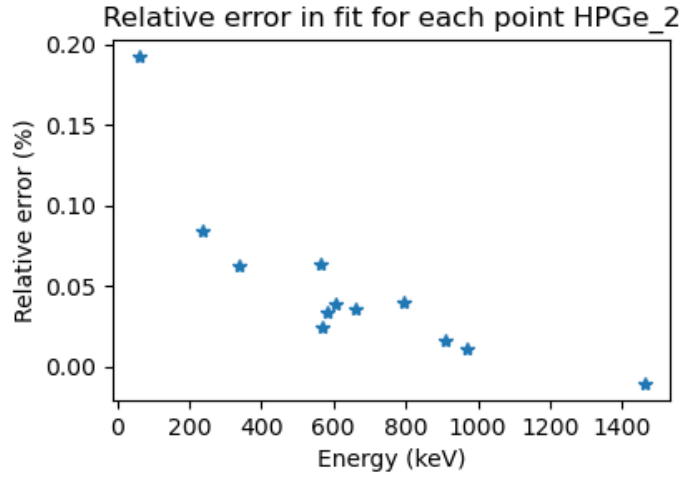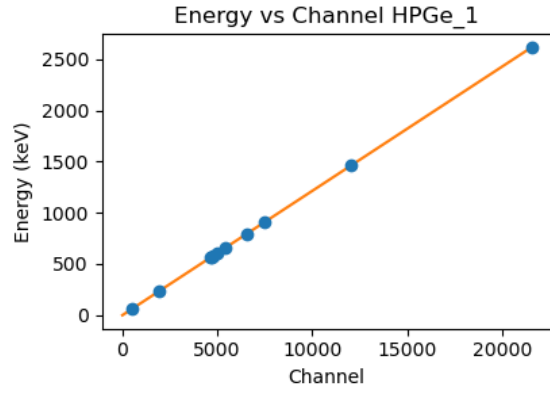

Figure 5.6: The normalized error between the linear fit and each point.

Table 5.5: The resulting parameters for the FWHM calibration for each detector.
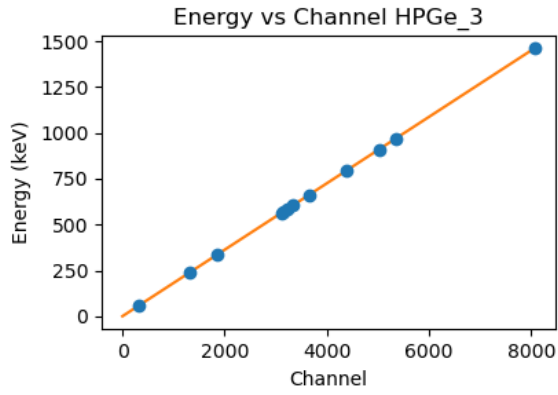
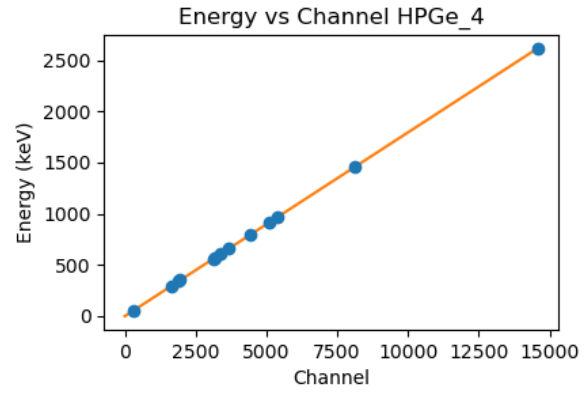| Detector	k (keV/keV)	m (keV)
1	$6,669969 \cdot 10^{-4} \pm 3,58 \cdot 10^{-8}$	$1,1661557 \pm 1,32 \cdot 10^{-5}$
2	$6,412052 \cdot 10^{-4} \pm 4,86 \cdot 10^{-8}$	$1,17998824 \pm 5,45 \cdot 10^{-6}$
3	$7,157581 \cdot 10^{-4} \pm 1,45 \cdot 10^{-8}$	$1,45649834 \pm 1,21 \cdot 10^{-6}$
4	$6,703638 \cdot 10^{-4} \pm 1,21 \cdot 10^{-8}$	$1,181032040 \pm 8,98 \cdot 10^{-7}$
5	$5,14093 \cdot 10^{-4} \pm 2,68 \cdot 10^{-7}$	$2,048825 \pm 0,000380$

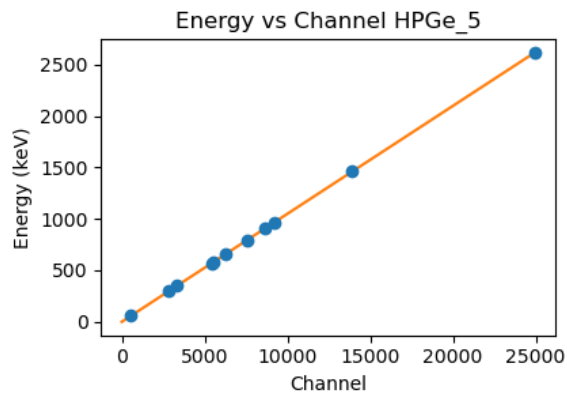(a) Energy calibration for detector 1.
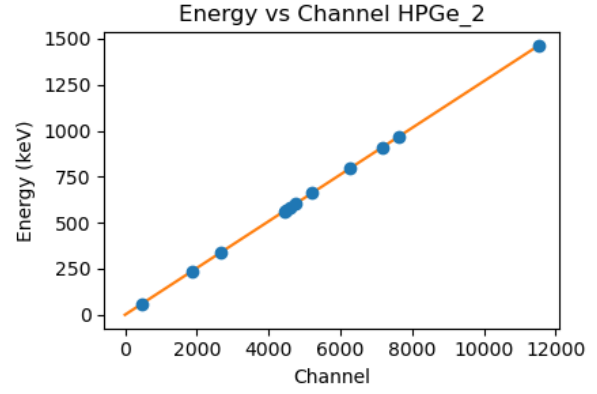
(b) Energy calibration for detector 2.

(c) Energy calibration for detector 3.

(d) Energy calibration for detector 4.

(e) Energy calibration for detector 5.

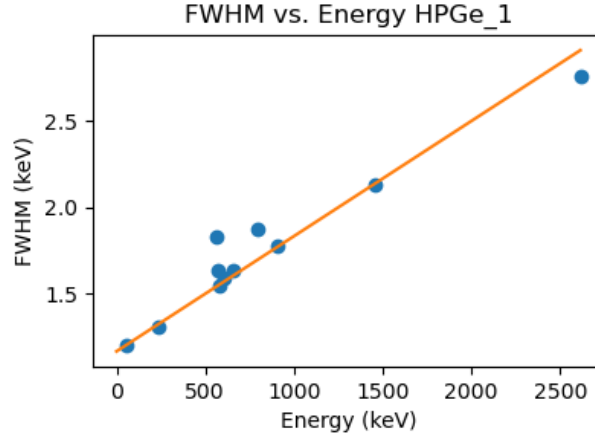Figure 5.7: Energy calibration for all five detectors.

Figure 5.8: FWHM depending on energy for detector 1.

For the efficiency, there were not enough data points to perform a calibration by fitting a function. Nevertheless, it was possible to calculate the efficiency for each peak and detector, using the method described in section 4.3. Before taking possible background peaks into account, the efficiency seemed to vary a lot and without much connection to the energy of the peak. After subtracting background peaks when relevant, the efficiency was more consistent throughout the peaks in each specific detector.

(a) Efficiency with correction.

(b) Efficiency without low energy.
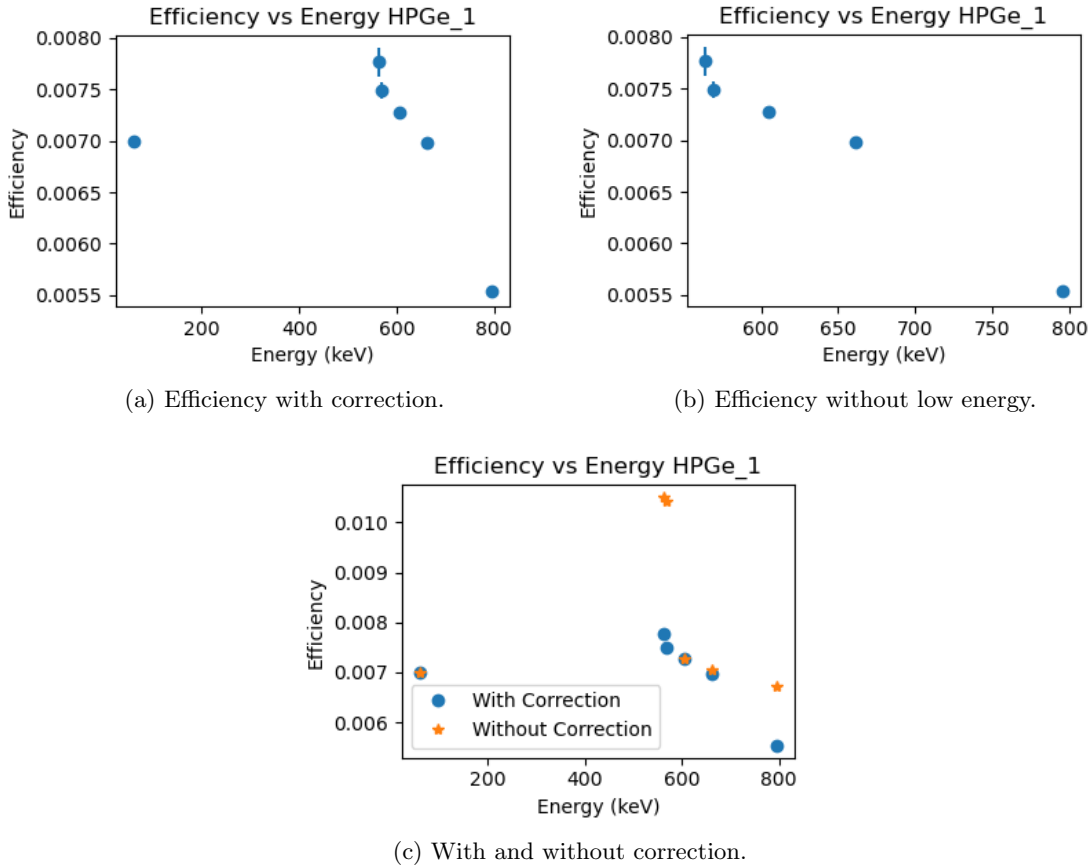

(c) With and without correction.

Figure 5.9: Efficiency for all peaks from the calibration sample, measured in detector 1.

In figure 5.9, the efficiency for detector 1 can be seen. In subfigure 5.9a, the result of the finished efficiency calculations can be seen, with regards to background peaks. In subfigure 5.9b, the value for the lowest energy has been removed. This value varied a lot compared to the others when observing different detectors and removal of this point was attempted to compare with the partially linear relationship that the efficiency is expected to have, see section 3.1.2. Subfigure 5.9c contains a juxtaposition between the efficiency before and after correction regarding background peaks. A comparison between the efficiency before and after background correction from figure 5.9c indicates that the background peaks had a significant impact on the efficiency through its impact on number of counts. The efficiencies for each peak in each detector can be found in table 5.6 together with energy, net peak counts and background counts.

Table 5.6: Information about counts and efficiency for relevant peaks in each detector. Background counts here quantifies the counts registered in the empty sample, used for background subtraction. Net peak counts is the net peak with subtraction for background counts.

Detector	Energy (keV)	Net Peak Counts Per Second	Efficiency	Background Counts Per Second
1	59,5409	2,9895	$0,007001 \pm 1,13 \cdot 10^{-4}$	3,1125
1	563,246	0,030140	$0,007764 \pm 5,63 \cdot 10^{-4}$	0,67862
1	569,331	0,055167	$0,007494 \pm 3,11 \cdot 10^{-4}$	0,10926
1	604,721	0,24476	$0,007280 \pm 1,30 \cdot 10^{-4}$	1,0383
1	661,657	1,4930	$0,006986 \pm 1,68 \cdot 10^{-4}$	2,4363
1	795,864	0,19756	$0,005544 \pm 1,09 \cdot 10^{-4}$	1,3122
2	59,5409	8,7663	$0,020530 \pm 3,30 \cdot 10^{-4}$	4,2376
2	563,246	0,021182	$0,005672 \pm 5,40 \cdot 10^{-4}$	0,64819
2	569,331	0,037984	$0,005620 \pm 2,45 \cdot 10^{-4}$	0,14494
2	604,721	0,18318	$0,0054482 \pm 9,72 \cdot 10^{-5}$	0,56049
2	661,657	1,0981	$0,005149 \pm 1,24 \cdot 10^{-4}$	0,39082
2	795,864	0,13882	$0,0040602 \pm 8,10 \cdot 10^{-5}$	0,43947
3	59,5409	24,503	$0,057384 \pm 9,22 \cdot 10^{-4}$	4,0780
3	563,246	0,042472	$0,013179 \pm 5,78 \cdot 10^{-4}$	0,72010
3	569,331	0,092682	$0,013078 \pm 3,69 \cdot 10^{-4}$	0,38408
3	604,721	0,42570	$0,012662 \pm 2,22 \cdot 10^{-4}$	0,38789
3	661,657	2,6834	$0,012580 \pm 3,02 \cdot 10^{-4}$	0,51158
3	795,864	0,29967	$0,009467 \pm 1,72 \cdot 10^{-4}$	0,38577
4	59,5409	26,249	$0,061472 \pm 9,87 \cdot 10^{-4}$	6,4709
4	563,246	0,039775	$0,012097 \pm 5,18 \cdot 10^{-4}$	0,45336
4	569,331	0,069382	$0,012002 \pm 4,16 \cdot 10^{-4}$	0,43949
4	604,721	0,40136	$0,011938 \pm 2,08 \cdot 10^{-4}$	0,39991
4	661,657	2,4652	$0,011616 \pm 2,79 \cdot 10^{-4}$	0,23297
4	795,864	0,28145	$0,008892 \pm 1,62 \cdot 10^{-4}$	1,8110
5	59,5409	1,0450	$0,0024473 \pm 3,97 \cdot 10^{-5}$	1,8097
5	569,331	0,078260	$0,005981 \pm 3,32 \cdot 10^{-4}$	0,86369
5	661,657	0,52539	$0,0024819 \pm 5,99 \cdot 10^{-5}$	0,26884
5	795,864	0,079987	$0,0023505 \pm 5,94 \cdot 10^{-5}$	0,57099

5.3   Coincidence Spectra

The 2-dimensional spectrum in the form of a histogram can be seen in figure 3.4 for detectors 3 and 4. A projection of the histogram onto detector 3 was made and can be seen in figure 5.10. This spectrum behaves much like the single detector spectra. A compton continuum is visible with the compton edge located around 450 keV.
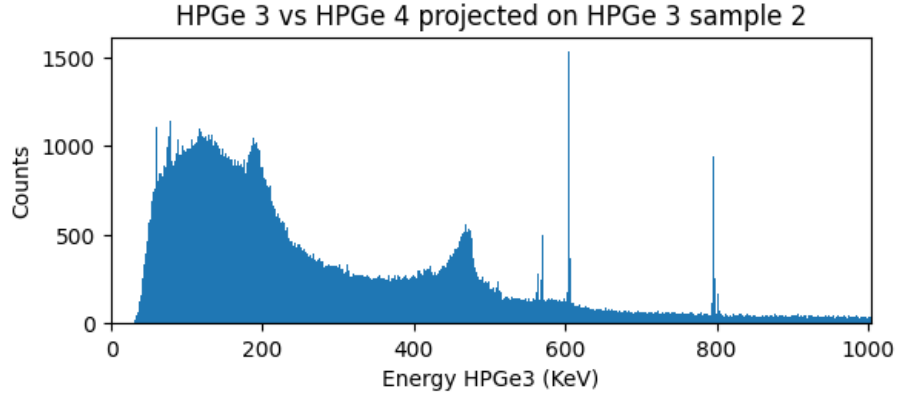
Figure 5.10: Coincidence spectrum from detectors 3 and 4 of data from calibration sample 2. A projection without gating has been made onto detector 3.

In figure 5.11, three different spectra from the same data with different sorting can be seen together. The top (blue) spectrum is the normal single spectrum of detector HPGe3. The spectrum in the middle (green) is the result of projecting the 2-D histogram of coincident events from between HPGe3 and HPGe4 onto HPGe3. The lowest spectrum (orange) is gated coincident events between HPGe3 and HPGe4 projected onto HPGe3.
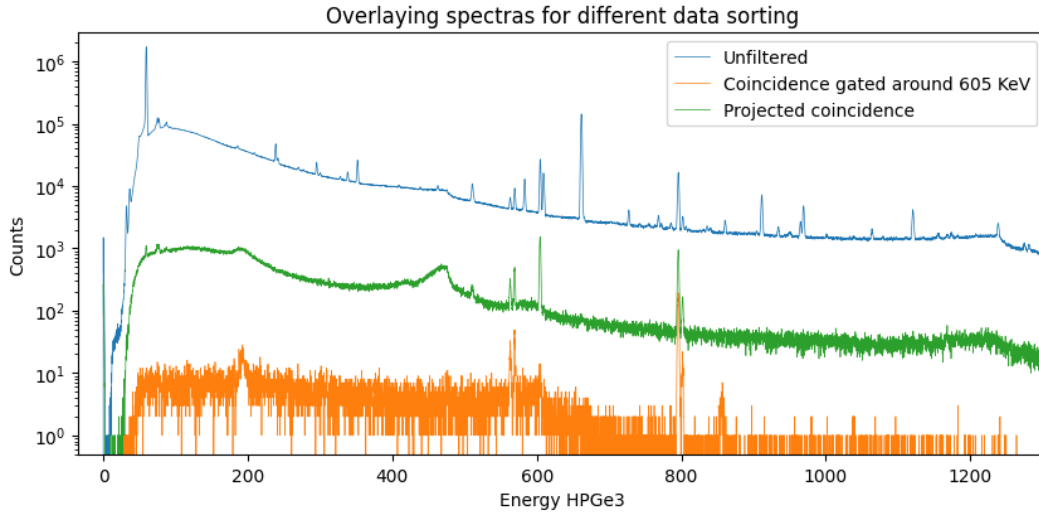

Figure 5.11: Three spectra plotted together using data from the same detector but three different levels of data sorting.

Figure 5.12, shows the same three spectra zoomed in around the 796 keV peak. To estimate the signal to noise ratio (SNR) Gedckes method was used to extract the met peak and background counts in all three spectra. SNR was calculated with the following expression.

$$SNR = \frac{\text{net peak counts}}{\text{background counts}} = \frac{c}{B} \tag{5.1}$$

The signal to noise rations are presented in table 5.7. The notation for the column spectrum type is as follows: the spectrum from the singular detector is called *Unfiltered*, the projected spectrum from the 2D histogram for coincidence without gating is referred to as *Projected* and the projection of the gated 2D histogram is referred to as *Gated*. As can be seen in the table, the number of counts in the net peak, and thus the

29

efficiency, is lowered for each filtering step. However, the background is lowered more and consequently the quotient increases.

Table 5.7: The number of counts in net peak and background and the quotient SNR for three different methods of data sorting.

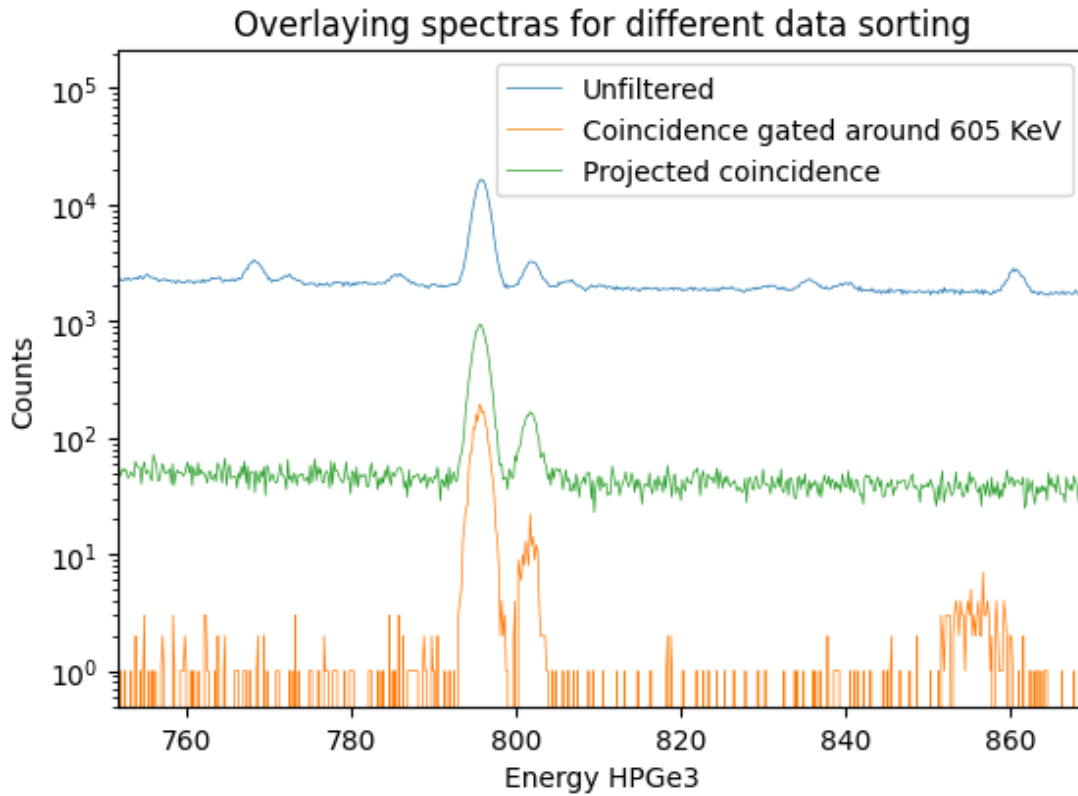| Type of Spectrum	Net Peak Counts	Background Counts	SNR
Unfiltered	178865	81345	2,20
Projected	10626	1773	9,06
Gated	2152	11	46,63

Figure 5.12: Three spectra plotted together using data from the same detector but different levels of data sorting. A closer look at the area around the 796 keV peak.

5.4   Coincidence Efficiencies

Coincidence efficiencies were calculated for each detector pair, excluding detector 5, for coincident decay energies 604,721 keV and 795,864 keV from ^{134}Cs. Table 5.8 presents the resulting coincidence efficiencies. Peak-peak counts were extracted with Gedckes method performed on the gated and projected spectra, as described in section 4.6. Efficiencies were calculated using equation 3.11 for each peak, with $I_{796,605} = 0.853$, $A = 34.441$ Bq and $T = 601088.6864$ s. Moreover, the product of the individual single efficiencies for the two energy detector pairs are presented, denoted $\varepsilon^A_{796/605} \cdot \varepsilon^B_{605/796}$ in equation (3.13). The correction term ρ is also calculated in the rightmost column of the table.

Table 5.8: Net peak counts, background counts, coincidence efficiency and correction term for each studied coincidence peak. Background counts is the sum of counts in the two background regions. In the gating process projections were always made on detector A.

Detector A	Detector B	Energy A (keV)	Energy B (keV)	Peak-Peak counts	Background counts	Coincidence efficiency	Efficiency product $(\varepsilon_A \cdot \varepsilon_B)$	Correction $\rho \pm \sigma_\rho$
HPGe1	HPGe2	796	604	454	7	$2,57 \cdot 10^{-5} \pm 0,12 \cdot 10^{-5}$	$3,020257 \cdot 10^{-5}$	$0,851 \pm 0,047$
HPGe1	HPGe2	604	796	391	4	$2,21 \cdot 10^{-5} \pm 0,11 \cdot 10^{-5}$	$2,955740 \cdot 10^{-5}$	$0,749 \pm 0,043$
HPGe1	HPGe3	796	604	1385	12	$7,84 \cdot 10^{-5} \pm 0,21 \cdot 10^{-5}$	$7,019052 \cdot 10^{-5}$	$1,117 \pm 0,042$
HPGe1	HPGe3	604	796	1387	6	$7,85 \cdot 10^{-5} \pm 0,21 \cdot 10^{-5}$	$6,891812 \cdot 10^{-5}$	$1,140 \pm 0,042$
HPGe1	HPGe4	796	604	1268	21	$7,18 \cdot 10^{-5} \pm 0,21 \cdot 10^{-5}$	$6,617762 \cdot 10^{-5}$	$1,085 \pm 0,042$
HPGe1	HPGe4	604	796	1202	6	$6,81 \cdot 10^{-5} \pm 0,20 \cdot 10^{-5}$	$6,472890 \cdot 10^{-5}$	$1,052 \pm 0,041$
HPGe2	HPGe3	796	604	990	9	$5,61 \cdot 10^{-5} \pm 0,18 \cdot 10^{-5}$	$5,140816 \cdot 10^{-5}$	$1,091 \pm 0,045$
HPGe2	HPGe3	604	796	927	10	$5,25 \cdot 10^{-5} \pm 0,18 \cdot 10^{-5}$	$5,157799 \cdot 10^{-5}$	$1,018 \pm 0,043$
HPGe2	HPGe4	796	604	878	4	$4,97 \cdot 10^{-5} \pm 0,17 \cdot 10^{-5}$	$4,846908 \cdot 10^{-5}$	$1,026 \pm 0,044$
HPGe2	HPGe4	604	796	932	4	$5,28 \cdot 10^{-5} \pm 0,17 \cdot 10^{-5}$	$4,844279 \cdot 10^{-5}$	$1,089 \pm 0,045$
HPGe3	HPGe4	796	604	2097	58	$11,88 \cdot 10^{-5} \pm 0,27 \cdot 10^{-5}$	$11,30140 \cdot 10^{-5}$	$1,051 \pm 0,036$
HPGe3	HPGe4	604	796	2258	13	$12,79 \cdot 10^{-5} \pm 0,28 \cdot 10^{-5}$	$11,25808 \cdot 10^{-5}$	$1,136 \pm 0,038$
Mean								$1,037$

Discussion

Many different background emissions with peaks at several energy levels were measured. A few of them were easily visible and consequently identified and used for energy calibration. As previously stated in section 5.1 there were also some background peaks interfering with our peaks of interest. Such background peaks were discovered for all ^{134}Cs peaks except one. A subsequent easy but false conclusion is that there is ^{134}Cs among the background emitters. There is however no reason that all energies but one should be visible, and that happening in five different detectors is highly unlikely and consequently, the only reasonable conclusion is that there is no background ^{134}Cs. All the interfering background peaks were instead from other background nuclides, not investigated further. For the analysis regarding coincident events, it was deemed not necessary to look at possible background subtraction before calculating the efficiency. Firstly this is because no coincident emitters were found in the background and therefore there should only be randomly coincident events in the background. Secondly, the probability of such random coincident events happening is small. Where there are a lot of events, like in the low-energy end of the spectrum, the probability increases but the interesting events were at a higher energy. However, it can be seen in section 5.2.3 and figure 5.9c that removing the background counts for single efficiency calculations had a large impact on the calculated efficiencies meaning that there were a lot of counts in the peak that were actually from the background. A small improvement to this project would be to check what nuclides could correspond to all the interfering background and see if there is some recommendation of shielding that can be done in preparation for future measurements.

Results from different methods of modeling net peaks in spectra were tested. Net peak counts with error bars from ROOT, SciPy and Gedcke methods are presented in figure 5.5. Using a curve fit approach, the choice of background intervals is not as sensitive since the actual background level beneath the Gaussian is always considered in calculations. Therefore the curve fit approach is considered to produce a more reliable result, and the error estimation to be more correct than that calculated with Gedckes method. When performing calibration on several detector elements, the extra labour of controlling each background level estimated with Gedckes method should also be considered a factor.

A more in depth comparison between the SciPy and ROOT algorithms was also conducted. Results from fitting a Gaussian with a superposed line in ROOT and SciPy are presented in table 5.2. For the Gaussian part, all parameters lie within one standard deviation. For the linear part, the parameters between the two do not lie within each others error margins, the reason for which is unknown. Presumably there is some difference in the algorithms performing the curve fit. For example one algorithm might weight the contribution of each point to the fit based on its error, while the other does not. This would give rise to different values. Performing the modified Gaussian curve fits in ROOT was considered the best option since it overall had a lower error on the estimated counts and thus gives more precise results. The ROOT interface was created to analyze data of this type and fitting Gaussian curves like what has been performed in this project is a common task performed in ROOT. On the other hand the SciPy library is more general and the algorithm used, very general. Perhaps the ROOT algorithm is optimized for finding Gaussian functions and therefore performs better. It is also possible that the ROOT iterative numerical solver does more iterations before returning parameters than the SciPy algorithm and therefore generates a better result.

The energy calibration resulted in a relationship between channel and energy which could later be used to convert between the two. The distance between the line and each calibration point was calculated and a plot can be seen in section 5.2.3, figure 5.6. Regarding the plot, it is important to first note that the

errors have been normalized, meaning that the difference in y between the regression line and each point is divided by the y value of the regression line. For clarification, for each x,y pair that has a point in the plot, the theoretical y value is calculated from the acquired relationship and the absolute difference between the actual y-value and the theoretical y-value is then divided by the theoretical y-value. This method usually results in a plot that can be used to spot a relationship between the normalized error and the x-value which is useful for example when deciding whether the fitting function needs an additional term or not. In this case, it can be seen that there is a relationship between the error and the x-value (channel). This is a strong indication that it might be a good idea to add a quadratic term to the fitting function. However, adding a quadratic term also has its problems. It can for example lead to overfitting and a worse prediction of y given x or vice versa. This is especially problematic towards the ends of the fitting interval or outside it where the fit can be completely different than the actual values. It is known that the channel and energy relationship for a detector is approximately linear, especially for large values. It should also be noted that the errors in the fit were very small and therefore, the fit was good. Since the fit was good and there are risks with adding a quadratic term, it was decided to keep the fitting function linear.

The FWHM calibration resulted in a linear relationship between the energy and FWHM. Theoretically, the fitting function is a little more complicated than a linear dependence on energy. The possibility of using such a more complicated fitting function was investigated, resulting in smaller errors and a more dynamic fit. The results can be found in appendix A.3. It was however noted that the result of the curve fit differed a lot between the detectors, some resulting in convex curves and others in concave. This was attributed to overfitting, a concept that describes when a model becomes too flexible, leading to poor generalization. Since overfitting is not desirable, it was decided that the linear approximation was a good fit for this project. Upon closer inspection, it can be seen that there are always the same two points slightly above the fit. No explanation has been found for this but it is clear that the linear curve fit would be a better fit to the remaining points if these two were removed. However, since there is no known reason for the two outliers, they cannot simply be ignored and are therefore still used in the fit.

There was an initial plan to also perform an efficiency calibration. The intended method for this was to calculate the efficiency for many different peaks and use regression to find some function that could describe the relationship between energy and efficiency. There were however not many active nuclides still in the sample and it was not possible to find a certain relationship between energy and efficiency. The efficiency for each peak was still calculated and used when comparing with the coincidence efficiencies. In figure 5.9 in section 5.2.3 it can be seen that if the point with the lowest energy is removed, the remaining five points show a seemingly linear relationship. This is interesting since theoretically, the energy and efficiency should have a partly linear relationship (for very low and high energies). The efficiency for 59 keV also varies a lot between the different detectors. This is due to the transmission fraction (see section 2.2.2) in the protective cover of the crystal being very sensitive in this energy region. Moreover the transmission decreasing in the detector cap and dead layer causes the theoretical efficiency function to be non linear in this energy region. The size of the detecting element in a detector is strongly connected to the efficiency. Here, the detecting elements are small and consequently, the efficiency is low. The results of the efficiency calibrations are therefore very reasonable despite the efficiencies being low.

In table 5.6 with the results of the efficiency calculations for the singular detector, the error in efficiency for each calculation is also displayed. Theoretically, the error in the number of counts should be about 0,1% since there are more than 100 000 counts [18]. The dominating contributor to the error in efficiency is the error in the original activity measurements. The errors for these measurements were between 1,6% and 2,4%, the same order of magnitude as the resulting efficiency errors. The resulting errors were found by error propagation, described in section 3.2, and should with the small errors in intensity, time measurements and number of counts, be only slightly larger than the error in the activity measurements. This is also what was observed, making the error in efficiency a reasonable size compared to the efficiency itself.

The coincidence efficiencies calculated in table 5.6 are small, however that is expected. The single efficiencies are small and thus the probability of detecting two coincident gamma rays is really small. Coincident events are less frequent than singular events and the number of peak-peak counts is smaller. Therefore a higher uncertainty permeates into the efficiency and correction term. Two hypotheses were presented based on the product of the singular efficiencies, with one containing a correction term. The first hypothesis that the coincidence efficiency is the product of the two single efficiencies is falsified by the presented results. There are no presented results to test the second hypothesis with the correction term against and it cannot

be confirmed nor denied. The presented correction terms can in the future be compared with theoretical studies of symmetry and with Monte Carlo simulations

An alternative to studying peak-peak efficiency is to study spectra like the one presented in figure 5.10, without gating before projection. This alternative will keep more counts and lower the relative statistical uncertainty by including Compton scattering events. This method needs a more complex analysis framework, including Compton scattering efficiencies. The three spectra presented in figure 5.11 and the signal to noise ratios (SNR) presented in table 5.7 show that sorting data on coincident events increases SNR. Given that the minimum detectable activity (MDA) is impaired by high background noise it is likely that the MDA is improved by studying coincident gamma rays.

6.1 Conclusion

A couple of things can be concluded from this project. Firstly, it was deduced that using ROOT to numerically fit a Gaussian curve to each peak was the best approach to model the net peaks. Using this approach the energy calibration was completed for each detector. The result is given by the parameters displayed in table 5.4 in section 5.2.3. Furthermore FWHM calibration was completed for each detector and the parameters are displayed in table 5.5 in section 5.2.3. Single efficiencies for all gamma energies emitted by the nuclides in the calibration sample were calculated and are presented in table 5.6 in section 5.2.3. Lastly, efficiencies for peak-peak coincident energies were calculated. The hypothesis that the coincidence efficiency is the product of the singular efficiencies was falsified by the presented results. The correction term relating the single efficiencies with the coincidence efficiency can be compared with future work. The signal to noise ratio improved when data was sorted on coincident events, and increased further when gating was performed.

Acknowledgements

References

[1] Peter Andersson. "Detection efficiency of a coincidence detection system with multiple detection elements". In: *Unpublished* (2024).

[3] Peter Andersson et al. "Coincidence spectroscopy for increased sensitivity in radionuclide monitoring". In: (2023).

[4] Philip R. Bevington and D. Keith Robinson. "Data reduction and error analysis for the physical sciences". eng. In: *Data reduction and error analysis for the physical sciences*. 3. ed. Boston: McGraw-Hill, 2003. ISBN: 0072472278.

[6] National Nuclear Data Center at Brookhaven National Laboratory. *NuDat3*. 2024. URL: https://www.nndc.bnl.gov/nudat3/ (visited on 04/04/2024).

[7] Alva Myrdal centre. *Arbetsgrupp 4: Teknisk icke-spridning och kärnämneskontroll.* (accessed: 22.05.2024). URL: https://www.uu.se/centrum/alva-myrdal/forskning/arbetsgrupp-4-teknisk-icke-spridning-och-karnamneskontroll.

[8] Comprehensive nuclear-test-ban treaty organisation preparatory commission. *Comprehensive Nuclear-Test-Ban Treaty (CTBT).* (accessed: 22.05.2024). URL: https://www.ctbto.org/sites/default/files/2023-10/2022_treaty_booklet_E.pdf.

[9] CTBTO Preparatory Commission. *ENDING NUCLEAR TESTS.* (accessed: 22.05.2024). URL: https://www.ctbto.org/our-mission/ending-nuclear-tests.

[10] Human Rights Foundation. *What is happening in China's concentration camps?* (accessed: 02.04.2024). URL: https://hrf.org/whats-happening-in-chinas-concentration-camps-qa-with-uyghur-camp-survivors/.

[11] Gordon. Gilmore. "Practical gamma-ray spectrometry". eng. In: *Practical gamma-ray spectrometry*. 2nd ed. Chichester, England ; John Wiley & Sons Ltd, 2008. Chap. 1. ISBN: 9780470861967.

[12] Gordon. Gilmore. "Practical gamma-ray spectrometry". eng. In: *Practical gamma-ray spectrometry*. 2nd ed. Chichester, England ; John Wiley & Sons Ltd, 2008. Chap. 2. ISBN: 9780470861967.

[14] Gordon. Gilmore. "Practical gamma-ray spectrometry". eng. In: *Practical gamma-ray spectrometry*. 2nd ed. Chichester, England ; John Wiley & Sons Ltd, 2008. Chap. 3. ISBN: 9780470861967.

[15] Gordon. Gilmore. "Practical gamma-ray spectrometry". eng. In: *Practical gamma-ray spectrometry*. 2nd ed. Chichester, England ; John Wiley & Sons Ltd, 2008. Chap. 7. ISBN: 9780470861967.

[17] Gordon. Gilmore. "Practical gamma-ray spectrometry". eng. In: *Practical gamma-ray spectrometry*. 2nd ed. Chichester, England ; John Wiley & Sons Ltd, 2008. Chap. 6. ISBN: 9780470861967.

[18] D. A. Gedcke. *ORTEC AN59 Application Note; How Counting Statistics Control Detection Limits and Peak Precision.* URL: https://www.ortec-online.com/-/media/ametekortec/application-notes/an59.pdf?la=en&revision=882b9886-9534-4c10-8e6f-b00c9703ed1e&hash604254C7CC458EC9B2%20CE0E90ED4FD2DC.

[19] Ruth Maclean. *What exactly is a Russian penal colony?* (accessed: 27.03.2024). URL: https://www.nytimes.com/2022/08/04/world/europe/russia-penal-colony-brittney-griner.html.

[20] Wolfram MathWorld. *Full Width at Half Maximum.* 2024. URL: https://mathworld.wolfram.com/FullWidthatHalfMaximum.html (visited on 05/03/2024).

[21] EU Non-Proliferation and Disarmament Consortium. *THE ALVA MYRDAL CENTRE FOR NU-CLEAR DISARMAMENT (AMC)*. (accessed: 22.05.2024). URL: `https://www.nonproliferation.eu/thinktanks-2/the-alva-myrdal-centre-for-nuclear-disarmament-amc/`.

[23] IAEA - Nuclear Data Section. *Live Chart of Nuclides*. 2024. URL: `https://www-nds.iaea.org/relnsd/vcharthtml/VChartHTML.html` (visited on 04/04/2024).

[24] Sveriges Geologiska Undersökning. *Germanium*. (accessed: 25.03.2024). URL: `https://www.sgu.se/mineralnaring/kritiska-ravaror/germanium/`.

[25] Wikipedia contributors. *Baruch Plan — Wikipedia, The Free Encyclopedia*. Online; (accessed 22.05.2024). 2023. URL: `https://en.wikipedia.org/w/index.php?title=Baruch_Plan&oldid=1173324097`.

Figure References

[2]   Peter Andersson. *Figures of GeCo*. Used with permission.

[5]   National Nuclear Data Center at Brookhaven National Laboratory. *NuDat3*. 2024. URL: `https://www.nndc.bnl.gov/nudat3/` (visited on 04/04/2024).

[13]   Gordon. Gilmore. "Practical gamma-ray spectrometry". eng. In: *Practical gamma-ray spectrometry*. 2nd ed. Chichester, England ; John Wiley & Sons Ltd, 2008. Chap. 2. ISBN: 9780470861967. Used with permission.

[16]   Gordon. Gilmore. "Practical gamma-ray spectrometry". eng. In: *Practical gamma-ray spectrometry*. 2nd ed. Chichester, England ; John Wiley & Sons Ltd, 2008. Chap. 7. ISBN: 9780470861967. Used with permission.

[22]   Arne Nordmann. *FWHM.svg*. Licensed under Creative Commons Attribution-ShareAlike 3.0 Unported: `https://creativecommons.org/licenses/by-sa/3.0/`. 2007. URL: `https://en.wikipedia.org/wiki/File:FWHM.svg` (visited on 03/05/2024).

Lay Summary

There are many treaties regarding testing and development of nuclear weapons and the subject of nuclear disarmament has constantly been a discussed political subject, ever since the first nuclear tests were conducted. To ensure that such nuclear disarmament treaties are followed, there must be techniques to discover nuclear weapon detonations. One part of such monitoring is an abundance of filter stations around the world. These filter stations consist of fans that sucks air through a filter resulting in particles getting stuck in the filter. Some particles are radioactive and decay to a state with extra energy, a so called excited state, later resulting in an energy release in the form of a gamma particle. The energy of such gamma particles are different and unique for each element. This offers the possibility of identifying an element based on its gamma energy. Thus by analyzing air filter samples, it is possible to determine what radioactive material is in the air. Certain elements are released at detonation of nuclear weapons and if they are found in higher concentrations in the air, it is almost certain that a nuclear detonation has taken place somewhere around the world. By having several such filter stations spread around the world it is also possible to determine the location of detonation.

To measure gamma energies and identify air particles in the filter, a detector is used. A detector often consist of a semiconducting material, a material that under certain conditions transmits a current. When a gamma particle interacts with the semiconductor it gives rise to an electrical signal with strength proportional to the energy of the gamma particle. In order to use a detector like this, it is necessary to know what current strength corresponds to which energy. This is done by calibrating the detector. Calibration is achieved by measuring on a sample with radionuclides of known properties to see what current strengths are achieved in a situation where the energy is known. With the help of these known current-energy pairs, a relationship between energy and current can be determined. One part of this project was to perform such an energy calibration, which resulted in a linear relationship between energy and current. This relationship can then be used to determine what energies of gamma particles are found in other filter samples and consequently, which particles currently exist in the air.

There is also another property of the detector that is of interest, the so called efficiency. Efficiency is a measurement of the amount of the present gamma particles that will actually be detected. In other words, the probability to detect a gamma particle given that it is released from the sample. The relationship between energy and efficiency can also be found by a calibration process. This relationship is not as simple as the linear relation between current and energy and can only be found if there are many known elements in the filter. The activity and intensity of these elements must be known to calculate the efficiency for a specific energy. The activity is the number of decays per second. The intensity is the probability that a gamma particle of a specific energy is emitted when a decay takes place. In this project, such properties were only known for six different energies, belonging to three different radionuclides. The efficiency was calculated for all these energies but no mathematical relationship could be found for such a limited amount of efficiency-energy pairs.

A problem that is sometimes encountered is the impact of background radiation, which can drown the interesting events. In this project, one way to lessen the impact of background radiation was investigated. It is called coincidence spectroscopy and focuses on so called coincident events. A coincident event in this case refers to an event where two or more gamma particles are emitted at the same time. There are several radionuclides that undergo such a process during decay, including some that are relevant for discovering nuclear weapon detonations. To measure coincident events, a new detector arrangement was founded with

four detectors horizontally aligned around a plastic can with a filter sample and one located above the plastic can. All data analyzed in this project came from measurements performed with this setup arrangement created under a project called GeCo (Germanium Coincidence). In the analyzed calibration sample, there was one common pair of coincident energies. For each possible detector pair, the efficiency (probability) of detecting this coincident energy pair was calculated. The coincidence efficiency was then compared to the hypothesis that the coincidence efficiency is the product of the singular efficiencies. Another hypothesis with a correction term to the aforementioned hypothesis was also proposed. The result being that one of the two hypotheses are plausible to explain the behaviour, however the statistical uncertainties were to large to give a definite answer.

Reflection regarding Sustainable Development

In this section there will be a reflection of this projects relation to sustainable development and to the United Nations 17 sustainable development goals. [1]

9.1 Goal 16: Peace, Justice and Strong Institutions

There have been many proposals regarding nuclear disarmament in the United Nations and it has resulted in adoption of the Treaty on the Prohibition of Nuclear Weapons and the Comprehensive Nuclear-Test-Ban Treaty (CTBT). The purpose of these treaties are to prevent nuclear wars and thus create a more safe and peaceful world. To enforce such treaties there must exist reliable detection systems that indicate breaches. The international monitoring system (IMS) was setup with this purpose and it, among other methods, makes use of gamma-ray spectrometry. In this report a detector is studied with the purpose of improving the minimum detectable activity, which is a measurement of how well a spectrometer performs. Contributing to better spectrometer devices thus improves future detection systems, which in turn means that there are more reliable indicators of nuclear weapon treaty breaches. Therefore this project contributes to the United Nations sustainability goal 16: Peace, Justice and Strong Institutions.

9.2 Indirect Consequences

Detonations of nuclear weapons result in devastation of nature and in radioactive carcinogenic material being spread over large areas. The aim is that this project will make some very small contribution to maintaining nuclear weapon treaties and thus reducing the usage of nuclear weapons. Furthermore the international monitoring center has been used to monitor whale behaviour and climate change, as well as by tsunami warning centers. Therefore this projected is related to contributions regarding development goals 13: Climate Action, 14: Life Below Water and 15: Life on Land.

9.3 Reflection on Germanium

Germanium is a critical material, a semiconductor with many modern applications. It is used for example in solar panels, electronics, catalysts and mainly fiber optics. Germanium is rare and a primary constituent in very few minerals. About half of the total germanium available can be found in Russia and 30% in China. The main producers are China (80%), Finland, Russia and Kazakhstan. [24]. All main producers, except Finland, have poorly regulated working conditions. Both China and Russia have work camps for prisoners, whom may or may not have committed breaches against the human rights, where both the working and living conditions are harsh. [19] [10]. Consequently, the project has a negative impact on the sustainable development goals 3: Good Health and Well Being and 10: Reduced Inequalities.

---

[1] More information regarding United Nations 17 sustainable development goals can be found on their website `https://sdgs.un.org/goals`.

There is always a risk when large parts of the world depend on only a few countries to produce a rare but needed semiconductor material like Germanium. This gives the countries in possession of the material a leverage whenever conflicts arises. It is difficult to demand something from someone you depend on. The project can thus be said to negatively impact sustainable development goal 12: Responsible Consumption and Production.

Appendices

A.1 Radionuclear Data

Radionuclide data from the nuclides in the two calibration samples were gathered and presented on the following page. Note that the data from calibration sample 1 was <u>not</u> used for the analysis presented in this report. The activity in sample one was last measured 2015-09-01 12:00:00 [UTC] and the activity in sample two measured 2013-03-01 12:00:00 [UTC]. Since then the activity has dropped according to equation (3.9). Measurements were carried out on sample 1 2024-01-29 and on sample 2 2024-01-26. The time difference between the two occasions are written in the top left corner of the next page. The half life was collected from IAEA Live Chart ([23]). Intensities and energies were gathered from NuDat 3 ([6]), for all decays with an intensity larger than 1%.Relative presence was calculated by multiplying intensity with activity and normalizing over the sample such that it summarizes to 100%. Relative presence thus represents the relative probability for a particular gamma to be emitted from the sample. Under Coincidence energies of gamma rays likely to be emitted at the same time are listed. Information about daughters were gathered and all daughters can be considered stable.

Time difference for calibration sample 1: 265161600s

Time difference for calibration sample 2: 344390400s

Nuclide	Last Known Activity		Half-life (s)	Activity During Calibration				Energy (keV)	Intensity (%)	Relative presence sample 1 (%)	Relative presence sample 2 (%)	Coincidence			Daughters
	Sample 1 (Bq)	Sample 2 (Bq)		Sample1 (Bq)	Standard deviation (Bq)	Sample 2 (Bq)	Standard deviation (Bq)					Energy 1	Energy 2	Energy 3	
			13651526177					26,3446	2,27	1,35	3,63				
Am-241	1090,906	1210,421		1076,317	17,450	1189,439	0,010	59,5409	35,9	21,38	57,46				237NP Stable
Cd-109	5552,432	10707,49	39908160	55,507	88,840	27,035	0,200	88,0336	3,644	0,11	0,13				109Ag Stable
Ce-139	268,531	380,449	11891232	0,000	4,300	0,000	0,000	165,8575	79,9	0,00	0,00				139La Stable
								122,06065	85,6	0,00	0,00				
								136,47356	10,68	0,00	0,00				
Co-57	203,496	279,345	23478336	0,081	0,001	0,011	0,011	14,4129	9,16	0,00	0,00				57Fe stable
								1173,228	99,85	20,22	0,00	1173,2	1332,5		
Co-60	1104,892		166344192	365,984	17,678			1332,492	99,9826	20,25	0,00				60Ni Stable
Cr-51	10559,411		2393626	0,000	0,000			320,0824	9,91	0,00	0,00				51V Stable
								569,331	15,373	0,00	0,71	569,331	795,864	604,721	
												801,953	563,246	604,721	
								801,953	8,688	0,00	0,40	801,953	1167,968		
								1365,185	3,017	0,00	0,14	1365,185	604,721		
												475,365	563,246	604,721	
								475,365	1,477	0,00	0,07	475,365	1167,968		
								795,864	85,46	0,00	3,96	795,864	604,721		
								563,246	8,338	0,00	0,39	563,246	604,721		
								1167,968	1,79	0,00	0,08				
Cs-134		1342,249	65171364			34,441	0,100	604,721	97,62	0,00	4,52				134Ba Stable
Cs-137	944,053	319,874	949232333	777,868	15,105	248,750	0,030	661,657	85,1	36,63	28,48				137Ba Stable
Hg-203		911,248	4027104			0,000	0,000	279,1952	81,56	0,00	0,00				203Tl Stable
Mn-54	832,165	765,541	26974080	0,914	0,010	0,110	0,001	834,848	99,976	0,05	0,01				54Cr Stable
								255,134	2,11	0,00	0,00	255,1	391,7		
Sn-113	979,018	754,362	9943776	0,000	0,000	0,000	0,000	391,698	64,97	0,00	0,00				113In Stable
Sr-85	1279,717		5602954	0,000	0,000			514,0048	96	0,00	0,00				85Rb Stable
								898,042	93,7	0,00	0,00	898,042	1836,063		
Y-88	2090,903	1399,992	9212486	0,000	0,000	0,000	0,000	1836,063	99,2	0,00	0,00				88Sr Stable
Zn-65	1937,058	2011,195	21075552	0,316	0,003	0,024	0,001	1115,539	50,04	0,01	0,00	770,6	344,95		64Cu Stable
										100,00	100,00				

A.2 Plots and Values

In figure A.1, the difference between fitting a linear function to the points received from the ROOT fits and the points received from the SciPy fits can be seen. Here the figures are for detectors 2-5, the figure for detector 1 is found in the result section.

Figure A.2 shows the normalized errors for the linear regression that constituted the energy calibration for detectors 1 and 3-5, the corresponding plot for detector 2 can be found in the result section. For the energy calibration, the full values (not rounded) for the parameters of the linear fit can be found in table A.1.

In figure A.3 all the FWHM for detectors 2-5 are visualised. The linear fitted function can be seen as well as the points used for the calibration. The FWHM for detector 1 can be seen in the result section.
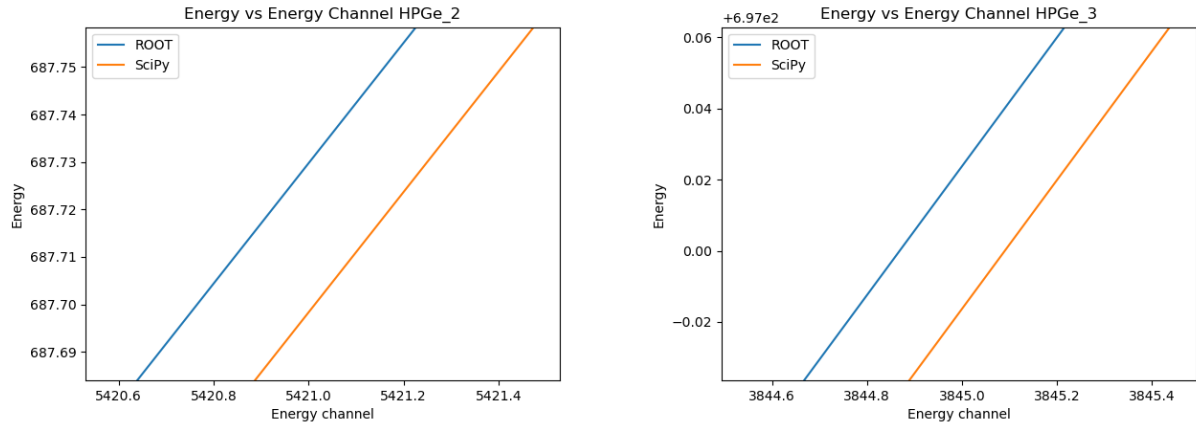
(a) A comparison between a fit using ROOT data points and a fit using SciPy data points for detector 2.

(b) A comparison between a fit using ROOT data points and a fit using SciPy data points for detector 3.
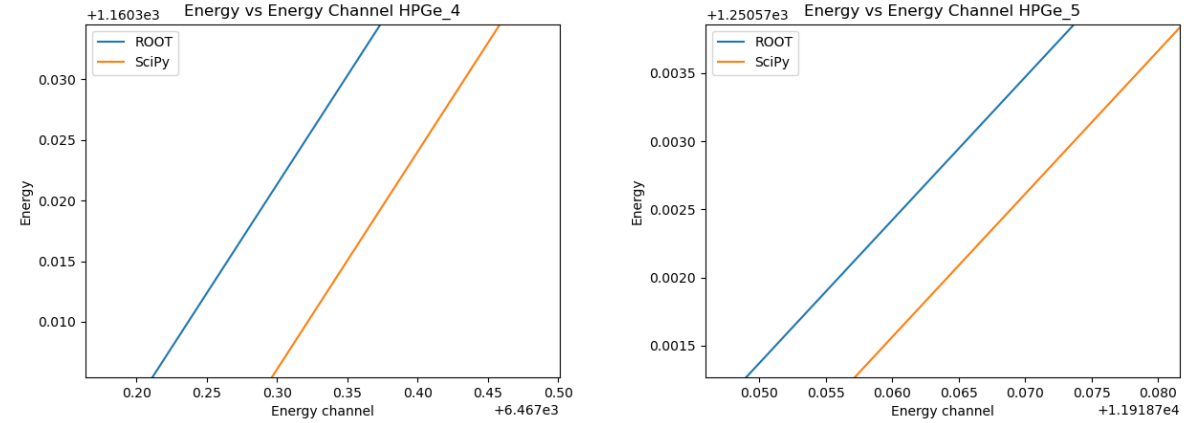
(c) A comparison between a fit using ROOT data points and a fit using SciPy data points for detector 4.

(d) A comparison between a fit using ROOT data points and a fit using SciPy data points for detector 5.

Figure A.1: Comparisons between fitting to the ROOT or SciPy data points.
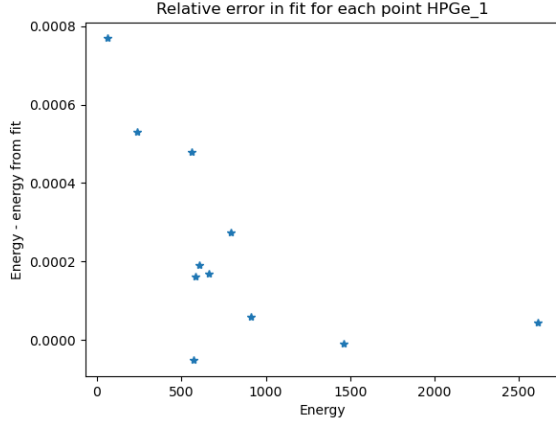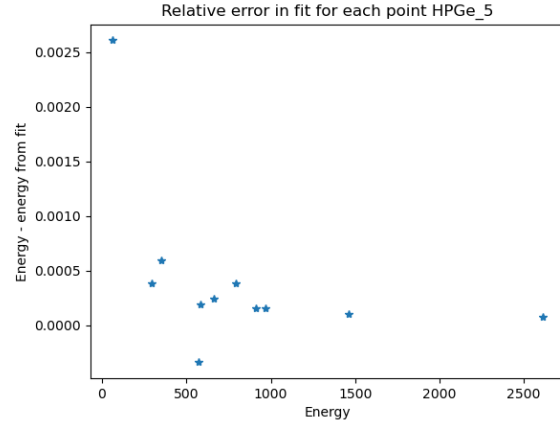
(a) The normalized difference between the fitted line and each data point for detector 1.
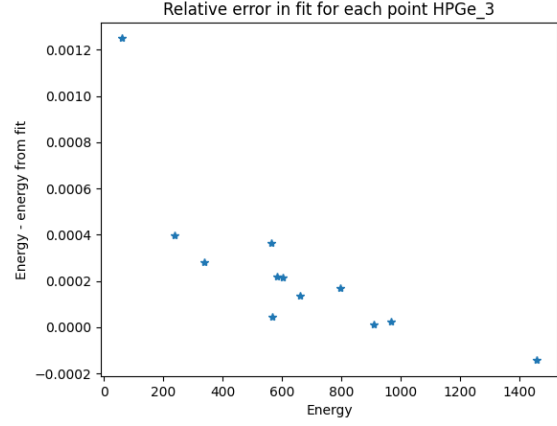
(b) The normalized difference between the fitted line and each data point for detector 3.
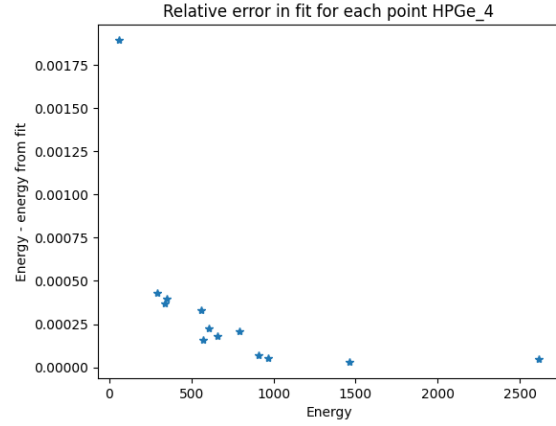
(c) The normalized difference between the fitted line and each data point for detector 4.

(d) The normalized difference between the fitted line and each data point for detector 5.

Figure A.2: Normalized error for the energy calibration for detectors 1 and 3-5.

Det	k	m
1	$0.12136658708907805 \pm 7.251712729058876 \cdot 10^{-10}$	$-0.024576563412505102 \pm 1.989084155296769 \cdot 10^{-6}$
2	$0.12685336718906823 \pm 1.1288801110661965 \cdot 10^{-9}$	$-0.057628701633824574 \pm 8.935873253988306 \cdot 10^{-7}$
3	$0.18127087994777463 \pm 7.611025613851137 \cdot 10^{-10}$	$-0.03723343542537557 \pm 3.3428046051665995 \cdot 10^{-7}$
4	$0.17940485210410242 \pm 5.91266921819476110^{-10}$	$-0.05633892698120359 \pm 2.425123273566940310^{-7}$
5	$0.10491824208477435 \pm 2.807854379684157310^{-9}$	$-0.07707412535464724 \pm 3.346966639294081610^{-5}$

Table A.1: The linear models achieved by energy calibration, full values.
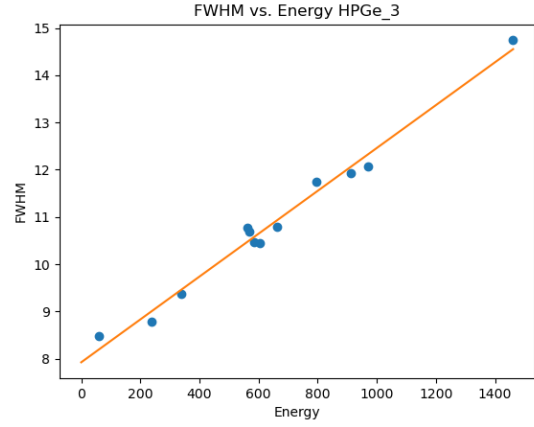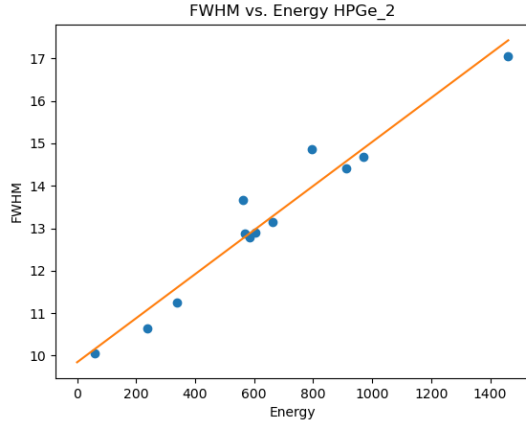
(a) Full Width Half Maximum calibration for detector 2. (b) Full Width Half Maximum calibration for detector 3.
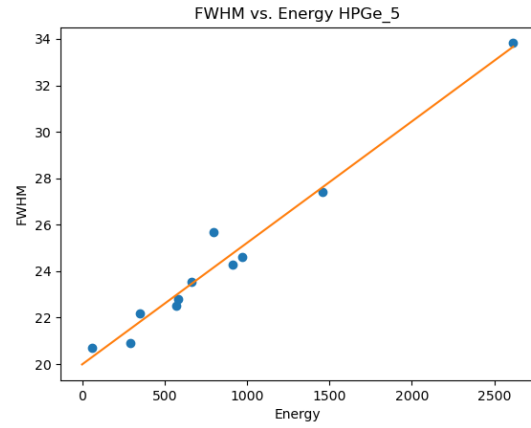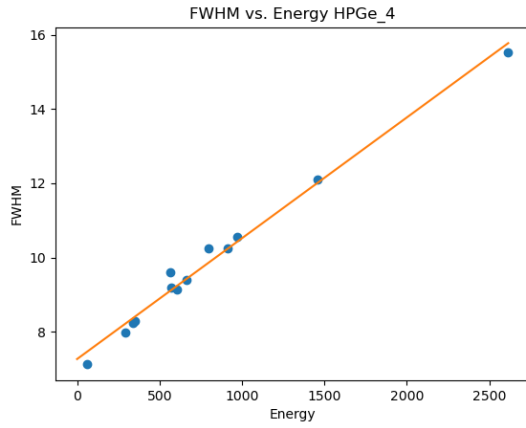
(c) Full Width Half Maximum calibration for detector 4. (d) Full Width Half Maximum calibration for detector 5.

Figure A.3: The Full Width Half Maximum calibrations for detectors 2-5. Both linear regression and calibration points shown in plot.

A.3 FWHM - Theoretical Function

Theoretically FWHM varies with energy according to the following relationship.

$$FWHM = \sqrt{e^2 + p^2 E + c^2 E^2} \tag{A.1}$$

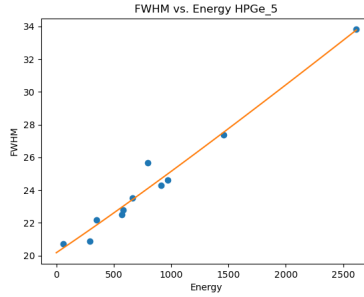where e, p and c are constant and E is the energy [17]. Regression was used to fit a curve of this form to the FWHM values. This resulted in convex and concave curves which is not desirable. The resulting fits were concave for detectors 1, 2 and 4 as seen in figures A.4a, A.4b and A.4d whereas figures A.4c and A.4e show that detectors 3 and 5 had convex fits of FWHM to energy.
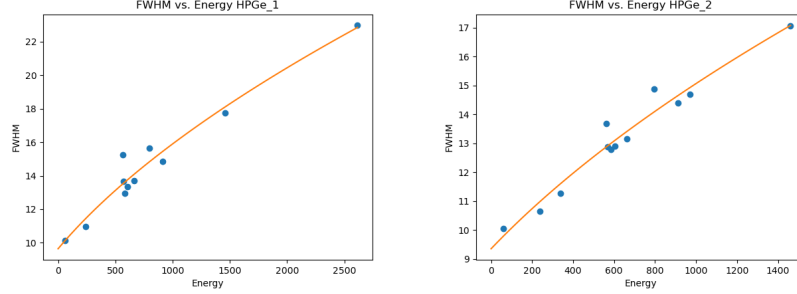
(a) Linear fitting between FWHM and energy for HPGe1

(b) Linear fitting between FWHM and energy for HPGe2
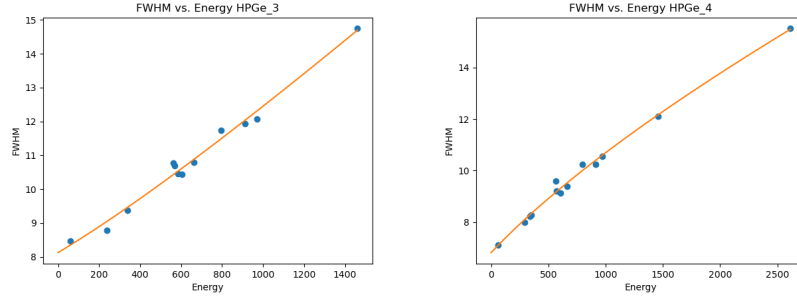
(c) Linear fitting between FWHM and energy for HPGe3

(d) Linear fitting between FWHM and energy for HPGe4

(e) Linear fitting between FWHM and energy for HPGe5